

SSC-441

**FIRE DEGRADATION, FAILURE
PREDICTION AND QUALIFICATION
METHODS FOR FIBER COMPOSITES**



This document has been approved
For public release and sale; its
Distribution is unlimited

SHIP STRUCTURE COMMITTEE
2005

SHIP STRUCTURE COMMITTEE

RADM Thomas H. Gilmour
U. S. Coast Guard Assistant Commandant,
Marine Safety and Environmental Protection
Chairman, Ship Structure Committee

Mr. W. Thomas Packard
Director,
Survivability and Structural Integrity Group
Naval Sea Systems Command

Dr. Jack Spencer
Senior Vice President
American Bureau of Shipping

Mr. Joseph Byrne
Director, Office of Ship Construction
Maritime Administration

Mr. Gerard A. McDonald
Director General, Marine Safety,
Safety & Security
Transport Canada

Mr. Thomas Connors
Director of Engineering
Military Sealift Command

Dr. Neil Pegg
Group Leader - Structural Mechanics
Defence Research & Development Canada - Atlantic

CONTRACTING OFFICER TECHNICAL REP.

Chao Lin / MARAD
Natale Nappi / NAVSEA
Robert Sedat / USCG

EXECUTIVE DIRECTOR
Lieutenant Eric M. Cooper
U. S. Coast Guard

SHIP STRUCTURE SUB-COMMITTEE

AMERICAN BUREAU OF SHIPPING

Mr. Glenn Ashe
Mr. Yung Shin
Mr. Phil Rynn
Mr. William Hanzalek

DEFENCE RESEARCH & DEVELOPMENT ATLANTIC

Dr David Stredulinsky
Mr. John Porter

MARITIME ADMINISTRATION

Mr. Chao Lin
Mr. Carlos Setterstrom
Mr. Richard Sonnenschein

MILITARY SEALIFT COMMAND

Mr. Joseph Bohr
Mr. Paul Handler
Mr. Michael W. Touma

NAVAL SEA SYSTEMS COMMAND

Mr. Jeffery E. Beach
Mr. Natale Nappi Jr.
Mr. Allen H. Engle
Mr. Charles L. Null

TRANSPORT CANADA

Mr. Jacek Dubiel

UNITED STATES COAST GUARD

Mr. Rubin Sheinberg
Mr. Robert Sedat
Captain Ray Petow

Member Agencies:

*American Bureau of Shipping
Defence Research Development Canada
Maritime Administration
Military Sealift Command
Naval Sea Systems Command
Society of Naval Architects & Marine Engineers
Transport Canada
United States Coast Guard*



**Ship
Structure
Committee**

Address Correspondence to:

Executive Director
Ship Structure Committee
U.S. Coast Guard (G-MSE/SSC)
2100 Second Street, SW
Washington, D.C. 20593-0001
Web site: <http://www.shipstructure.org>

**SSC - 441
SR - 1397**

MAY 2005

**FIRE DEGRADATION, FAILURE PREDICTION AND QUALIFICATION METHODS FOR
FIBER COMPOSITES**

This research report is concerned with the effects of fire on the structural integrity of composite materials. The research was initiated to develop and implement advanced composites for ship design and construction. This report focused on the development of a quantitative framework assessing the degradation of composite material properties and the resulting degradation in the structural integrity of composite structures. Our approach characterizes the thermal degradation of elastic-viscoplastic properties of advanced composites, to develop models for their temperature and time dependent behavior, and conduct combined experimental-theoretical studies of the behavior of thermally degraded composite structures. An important underlying component of our studies is characterizing, and modeling, the micro- and macromechanical failure processes that lead to structural failure. The other component of our work is the quantitative description of structural collapse which can serve as the basis of a design methodology.

A handwritten signature in black ink, appearing to read 'T. H. Gilmour', written in a cursive style.

T. H. GILMOUR

Rear Admiral, U.S. Coast Guard
Chairman, Ship Structure Committee

Technical Report Documentation Page

1. Report No. SSC-441		2. Government Accession No. PB2005-108997		3. Recipient's Catalog No.	
4. Title and Subtitle Fire Degradation, Failure Prediction and Qualification Methods For Fiber Composites				5. Report Date May 2005	
				6. Performing Organization Code	
7. Author(s) Asaro, R.J.; Dao M.				8. Performing Organization Report No. SR-1397	
9. Performing Organization Name and Address University of California, San Diego Dept. of Structural Engineering La Jolla, CA 92093				10. Work Unit No. (TRAIS)	
				11. Contract or Grant No.	
12. Sponsoring Agency Name and Address Ship Structure Committee U.S. Coast Guard (G-MSE/SSC) 2100 Second Street, SW Washington, DC 20593				13. Type of Report and Period Covered Final Report	
				14. Sponsoring Agency Code G-M	
15. Supplementary Notes Sponsored by the Ship Structure Committee. Jointly funded by its member agencies.					
16. Abstract Developments in advanced composite fabrication technology offer the clear prospect of cost effective application of polymer matrix composites for large load bearing structures, including ship and civil structures such as piers and bridges. However, polymer matrix composites can be severely degraded (damaged) under the thermal loading caused by fire. This report describes results from combined experimental and theoretical studies of compressive failures of polymer matrix glass reinforced composites which have undergone fire degradation. Both single skin and cored composites materials are addressed in our studies. Experimental studies have been conducted on composite panels of approximately 1m squared in size. These investigations have documented the structural collapse of the panels when they are subjected to combined thermal (i.e. fire) loading and in-and out-of-plane mechanical loading. Detailed finite element simulations, performed in parallel with analytical modeling, of panel deformation and collapse show good agreement with the experimental observations. The approach to the development of a quantitative methodology for structural fire protection is discussed in the context of the experiments and these analyses. Finally, simple design approaches are proposed for single and cored panels and discussed with respect to experimental results and thermal boundary conditions.					
17. Key Words composite, thermal load, polymer matrix composites			18. Distribution Statement Distribution is available to the public through: National Technical Information Service U.S. Department of Commerce Springfield, VA 22151 Ph. (703) 487-4650		
19. Security Classif. (of this report) Unclassified		20. Security Classif. (of this page) Unclassified		21. No. of Pages 123	22. Price \$34.00 paper \$14.00 microfiche

CONVERSION FACTORS
(Approximate conversions to metric measures)

To convert from	to	Function	Value
LENGTH			
inches	meters	divide	39.3701
inches	millimeters	multiply by	25.4000
feet	meters	divide by	3.2808
VOLUME			
cubic feet	cubic meters	divide by	35.3149
cubic inches	cubic meters	divide by	61,024
SECTION MODULUS			
inches ² feet ²	centimeters ² meters ²	multiply by	1.9665
inches ² feet ²	centimeters ³	multiply by	196.6448
inches ⁴	centimeters ³	multiply by	16.3871
MOMENT OF INERTIA			
inches ² feet ²	centimeters ² meters	divide by	1.6684
inches ² feet ²	centimeters ⁴	multiply by	5993.73
inches ⁴	centimeters ⁴	multiply by	41.623
FORCE OR MASS			
long tons	tonne	multiply by	1.0160
long tons	kilograms	multiply by	1016.047
pounds	tonnes	divide by	2204.62
pounds	kilograms	divide by	2.2046
pounds	Newtons	multiply by	4.4482
PRESSURE OR STRESS			
pounds/inch ²	Newtons/meter ² (Pascals)	multiply by	6894.757
kilo pounds/inch ²	mega Newtons/meter ² (mega Pascals)	multiply by	6.8947
BENDING OR TORQUE			
foot tons	meter tons	divide by	3.2291
foot pounds	kilogram meters	divide by	7.23285
foot pounds	Newton meters	multiply by	1.35582
ENERGY			
foot pounds	Joules	multiply by	1.355826
STRESS INTENSITY			
kilo pound/inch ² inch ^{1/2} (ksi ^{1/2} /in)	mega Newton MNm ^{3/2}	multiply by	1.0998
J-INTEGRAL			
kilo pound/inch	Joules/mm ²	multiply by	0.1753
kilo pound/inch	kilo Joules/m ²	multiply by	175.3

Contents

1	Introduction	9
1.1	General Background	9
1.2	Current Status	9
1.3	Future Regulatory Directions	10
1.4	Basic Objectives and Procedures	11
2	Description of Materials and Thermal Properties	12
2.1	Material Descriptions	12
2.2	Thermal Properties of High-Fiber Density Materials and a Master Degradation Curve	12
2.3	Thermal Properties of High-and-Low-Fiber Density Materials	13
2.3.1	Material and Test Methodology	13
2.3.2	Material Test Results and Discussions	13
3	Standards for Alloy Construction and Overall Approach	15
4	Failure Modes and Mechanisms in FRP Composites	16
5	Experimental Procedures for Testing Panels Under Compressive Loading	17
5.1	High-Fiber Density Panel Architecture	17
5.2	Low-Fiber Density Panel Architecture	17
6	A Single Skin Model	18
6.1	A Simple Collapse Model	18
6.2	Micromechanical Considerations	19
7	Single Skin Model Analyses and Experimental Results	20
7.1	Thermal Analysis and Case 1 (High-Fiber Density Materials)	20
7.2	Material Degradation Profile for Case 1 (High-Fiber Density Materials)	20
7.3	Structural Analysis of Case 1 (High-Fiber Density Materials)	21
7.4	A Two-Parameter Model and Analysis of Case 1 (High-Fiber Density Materials)	21
7.5	Case 2 (High-Fiber Density Materials)	22
7.6	Case 3 and 4 (Low-Fiber Density Materials)	22
8	Discussion on Design Criteria for Single Skin Panels	23
8.1	General Discussion	23
8.2	Single Skin Design and Test Methodology	24
8.3	A Simple Single Skin Test with Validation	24
9	Failure Modes in Sandwich Panels	26
9.1	Perspective on Sandwich Panel Failures	26
9.2	Finite Element Results	27
9.2.1	Wrinkling Load versus Imperfection and Core Thickness	27
9.2.2	Failure Mode Change with Core Thickness	27
9.2.3	Failure Mode Change with Core Thickness	28
10	Simplified Damage Models for Sandwich Panels	29
10.1	A Simplified Damage Model for Short Sandwich Panels	29
10.2	A Simplified Damage Model for Slender Sandwich Panels	29
10.2.1	Experimental Results for Slender Sandwich Panels (High-Fiber Density Materials)	29
10.2.2	A Simplified Thermal Profile Model	30
10.2.3	Experimental Results for Slender Sandwich Panels (Low-Fiber Density Materials)	31
10.3	Experimental Results for Slender Sandwich Panels (Low-Fiber Density Materials)	31

11 Sandwich Panel Design and Test Methodology	32
11.1 Background Discussion	32
11.2 Sandwich Panel Methodology	32
11.2.1 A Simple Sandwich Panel Test with Validation	33
12 Conclusions	34
13 Recommendations for Future Work	35
13.1 Validation <i>vis-a-vis</i> Stiffened Panels	35
13.2 Validation <i>vis-a-vis</i> Fully 3-D Structures	35
13.3 Material Properties and Hybrid Materials	35
13.4 Residual Structural Performance	35
13.5 Structural Fire Protection Code Development	36
14 Acknowledgements	37
15 References	38
16 Appendix	39

List of Figures

1. Figure 1. Property Degradation Curves for (a) E-glass vinylester skin material, (b) PVC core material, and (c) core material; χ and χ_o represent properties such as stiffness or interlaminar shear as they depend on temperature and their initial state respectively, (d) shows the residual property degradation data for E-glass skin material.
2. Figure 2. Residual normalized tensile strength for composite fabricated from 2 quadriaxial nonwoven QM5708 impregnated with Corezyn Vinylester using wet layup process and vacuum bagging.
3. Figure 3. Normalized tensile strength from testing at temperature for composite fabricated from 2 quadriaxial nonwoven QM5708 impregnated with Corezyn Vinylester using wet layup process and vacuum bagging.
4. Figure 4. Normalized tensile strength from testing at temperature for VEX19-540 specimen fabricated using SCRIMP.
5. Figure 5. Normalized tensile strength from testing at temperature for VEX159-540 specimen fabricated using SCRIMP.
6. Figure 6. Residual normalized tensile strength for needle-punched specimen fabricated using SCRIMP.
7. Figure 7. Normalized tensile strength from testing at temperature for needle-punched specimen fabricated using SCRIMP.
8. Figure 8. Residual normalized tensile strength for a Woven roving-chopped strand mat configuration specimen fabricated using SCRIMP.
9. Figure 9. Residual normalized compressive strength for a Woven roving-chopped strand mat configuration specimen fabricated using SCRIMP.
10. Figure 10. Residual normalized tensile strength for XM fabric and CIBA resin fabricated using SCRIMP.
11. Figure 11. Residual normalized compressive strength for XM fabric and CIBA resin fabricated using SCRIMP.
12. Figure 12. Residual normalized tensile strength for a specially formulated fire-resistant resin specimen fabricated with wet layup process.
13. Figure 13. Residual normalized compressive strength for a specially formulated fire-resistant resin specimen fabricated with wet layup process.
14. Figure 14. Residual normalized flexural strength for a specially formulated fire-resistant resin specimen fabricated with wet layup process.
15. Figure 15. Normalized flexural strength from testing at temperature for a specially formulated fire-resistant resin specimen fabricated with wet layup process.
16. Figure 16. Temperature dependent variation of yield and ultimate tensile strengths for elastic-plastic buckling analysis of 6061 aluminum alloy panels.
17. Figure 17. Variations of critical collapse stress, *i.e.* “collapse load” averaged over the area of the panel cross-section $P_{coll}/(wh)$ for elastic-plastic buckling analysis of 6061 aluminum alloy panels.
18. Figure 18. Modeling approach.
19. Figure 19. Failure mechanisms in composites. E_f and E_c are sandwich “face” and “core” stiffness respectively. τ_y is the interlaminar shear strength and τ_∞ the remotely applied shear stress. G_c is the in-plane shear stiffness of the “core” material, and E is again the “face” stiffness

20. Figure 20. Multi-axial loading jig.
21. Figure 21. A simple collapse model with material property variation.
22. Figure 22. Thermal analysis results from Case 1: (a) temperature *versus* time plots at different panel positions, and (b) temperature distributions profiles at different fire exposure times.
23. Figure 23. Through-thickness degradation profiles at different times for Case 1.
24. Figure 24. Calculated critical collapse load *versus* fire expose time along with measured out-of-plane displacement *versus* time for Case 1.
25. Figure 25. Thermal analysis results from Case 2: (a) temperature *versus* time plots at different panel positions, and (b) temperature distributions profiles at different fire exposure times.
26. Figure 26. Through-thickness degradation profiles at different times for Case 2.
27. Figure 27. Calculated critical collapse load *versus* fire expose time along with measured out-of-plane displacement *versus* time for Case 2.
28. Figure 28. Calculated critical collapse load *versus* fire expose time along with measured out-of-plane displacement *versus* time for Case 3.
29. Figure 29. Calculated critical collapse load *versus* fire expose time along with measured out-of-plane displacement *versus* time for Case 4.
30. Figure 30. Critical collapse load *versus* center temperature T_c for Case 1.
31. Figure 31. Critical collapse load *versus* center temperature T_c for Case 2.
32. Figure 32. (a) Temperature distribution profiles at different fire exposure times with $\dot{q} = 3kw/m^2$, obtained by solving the thermal boundary value problem described in the insert; and (b) incident heat flux needed versus the times it takes to achieve different panel center temperatures.
33. Figure 33. Schematic drawing of a proposed simple thermal screening test setup for single skin panels.
34. Figure 34. When $T_c = 110^\circ C$ is specified for a single skin panel, the measured T_c *versus* time cure can be plotted. The specified, or desired fire protection time must be less than t_{max} as illustrated in the figure. The ambient temperature is $20^\circ C$.
35. Figure 35. Critical load versus core thickness. The panel skin thicknesses are taken as $f \approx 1.5mm$ ($0.6in$) and the length as $L = 0.38m$ ($15in$).
36. Figure 36. Schematic drawings of (a) sandwich panel property degradation, and (b) a simplified damage model for sandwich panels.
37. Figure 37. (a) Undeformed, and (b) deformed mesh of the partially damaged sandwich panel.
38. Figure 38. Critical load *versus* the extent of damage c_d and the damaged modulus E_{core} . E_{core}^0 is the undamaged core modulus.
39. Figure 38. (a) Thermal couple positioning, and the corresponding gradients developed in the sandwich panel. (b) Simplified linear temperature distribution model, where temperature T_b at the exposed face/core interface becomes the most important parameter.
40. Figure 40. Measured temperature profiles as functions of time within the composite sandwich panel for (a) Case 5 airlite foam core, (b) Case 6 airlite foam core and (c) Case 7 balsa core, respectively.
41. Figure 41. Measured vertical displacement *versus* time curves along with the calculated maximum sustainable load *versus* time for (a) Case 5 airlite foam core, (b) Case 6 airlite foam core and (c) Case 7 balsa core, respectively.

42. Figure 42. Thermal conductivity calculations. (a) = $1kw/m^2$, with 5.08 mm (0.2in) thick skins and a 25.4mm (1 in) thick core. (b) = $3kw/m^2$, with 5.08 mm (0.2in) thick skins and a 25.4mm (1 in) thick core. (c) = $1kw/m^2$, with 7.62 mm (0.3in) thick skins and a 25.4mm (1 in) thick core. (d) = $1kw/m^2$, with 7.62 mm (0.3in) thick skins and a 50.8mm (2 in) thick core.
43. Figure 43. Measured vertical displacement versus time curves along with the calculated maximum sustainable load *versus* time for (a) Case 5 airlite foam core and (b) Case 7 balsa core, respectively. The simplified linear model shown with solid lines gives excellent approximations as compared to the original model.
44. Figure 44. Calculated collapsed load *versus* fire exposure time along with measured out-of-plane displacement for Case 8.
45. Figure 45. Calculated collapsed load *versus* fire exposure time along with measured out-of-plane displacement for Case 9.
46. Figure 46. Measured temperatures *versus* time for Case 6 at various locations through the panel thickness and those computed *via* a thermal analysis.
47. Figure 47. Results of a series of finite element calculations on sandwich panels whose dimensions are listed in the inserted table. This set of calculations were performed using the simplified linear temperature distribution model.
48. Figure 48. Schematic drawing of a proposed simple thermal screening test setup for sandwich panels.

List of Tables

1	Excerpts from the CFR	10
2	Critical Wrinkling Load <i>Versus</i> Imperfection and Core Thickness. For all cases shown in this table the skin thickness was taken as $f \approx 1.5mm$ (0.6in)	27

Abstract

Developments in advanced composite fabrication technology offer the clear prospect of cost effective application of polymer matrix composites for large load bearing structures, including ship and civil structures such as piers and bridges. However, polymer matrix composites can be severely degraded (*damaged*) under the thermal loading caused by fire. This report describes results from combined experimental and theoretical studies of compressive failures of polymer matrix glass reinforced composites which have undergone fire degradation. Both *single skin* and *cored* composites materials are addressed in our studies. Experimental studies have been conducted on composite panels of approximately $1m^2$ in size. These investigations have documented the structural collapse of the panels when they are subjected to combined thermal (*i.e.* fire) loading and in-and out-of-plane mechanical loading. Detailed finite element simulations, performed in parallel with analytical modelling, of panel deformation and collapse show good agreement with the experimental observations. The approach to the development of a quantitative methodology for structural fire protection is discussed in the context of the experiments and these analyses. Finally, simple design approaches are proposed for single and cored panels and discussed with respect to experimental results and thermal boundary conditions.

1 Introduction

1.1 General Background

Advanced fiber composites are becoming cost effective in applications involving smaller ships and large load bearing structures for large vessels. Fire protection concerns, however, have limited U.S. domestic applications to only small passenger vessels of less than 65 feet in length, under 100 gross tons, and which carry less than 15 passengers. Developments in advanced composite fabrication technology and fire protection materials permit this to safely occur. For reasons of performance and cost effectiveness, there is reason to expand the domestic use of composites to larger vessels, but this requires the development of a quantitative methodology for analyzing the response of composite structures to fire.

International regulations and standards are defined by the International Maritime Organization (IMO) through the International Convention for the Safety of Life at Sea (SOLAS). Currently these standards require construction using steel or equivalent materials in conjunction with insulation. Aluminum alloys have been determined to be equivalent to steel, provided sufficient insulation materials are installed to protect the structural elements, whereas other materials have not met the standards due to their inherent combustibility. The recently issued IMO High Speed Craft Code [1] does allow the use of combustible structural materials provided they qualify as *fire restricting* and can be used to form *fire resistant divisions*. Standards for these in terms of material combustibility properties, and fire related structural integrity, have been or are current under development by the IMO. Principal concerns of both domestic and international regulations are that the materials used for construction will not themselves contribute inordinately to the fire in terms of heat and smoke release not that the structures will display adequate structural integrity during, and after, fire induced thermal loading.

The research reported on below is concerned with the effects of fire on the structural integrity of composite materials. The research was begun as part of a program conducted at the University of California, San Diego (UCSD), sponsored under the DARPA MARITECH initiative to develop and implement advanced composites for ship design and construction. Specifically, the work discussed here had focused on the development of a quantitative framework assessing the degradation of composite material properties and the resulting degradation in the structural integrity of composite structures. Our approach has been to characterize the thermal degradation of elastic-viscoplastic properties of advanced composites, to develop models for their temperature and time dependent behavior, and conduct combined experimental-theoretical studies of the behavior of thermally degraded composite structures. An important underlying component of our studies is characterizing, and modelling, the micro- and macromechanical failure processes that lead to structural failure. The other component of our work is the quantitative description of structural collapse which can serve as the basis of a design methodology. Additional background discussion, and our first reports, can be found in Asaro and Dao *et. al.* [2] [3].

1.2 Current Status

The current international and domestic requirements for fire protection on vessels has a long history dating back to the Second International Convention for the Safety of Life at Sea (SOLAS) in 1929 which required construction with “fire-resisting bulkheads.” The Fire Proofing and Fire Prevention Group, which was then established, determined that the best method for controlling fire spread “would be construction if such nature that it would confine any fire to the enclosures in which it originated.” This concept of “passive” fire protection has become one of the fundamental principles of structural fire protection in both SOLAS and US regulations today.

Starting in 1936, a series of fire tests were conducted on board a test ship SS NANTASKET which resulted in a form of construction in which combustible materials were largely eliminated. In April 1948, many of these findings were incorporated into international regulations at the third SOLAS Convention. Two later conventions, SOLAS 60 and SOLAS 74, added further improvements to international structural fire protection requirements. Today, the structural fire protection philosophy is based on many full scale tests as well as on design guidelines concerned with structural design and fire protection and extinguishing systems.

Table 1: Excerpts from the CFR

Vessel Type	Regulation Cite	Construction Requirement
Tank Vessel	46 CFR 32.51-10	Steel or other suitable material having in mind the risk of fire
Large Passenger Vessel	46 CFR 72.05-10	Steel or other equivalent material
Cargo Vessel	46 CFR 92.07-10 (a)	Steel or other suitable material having in mind the risk of fire
MODU	46 CFR 208.133	Steel or other equivalent material
Small Passenger Vessel >150 Passengers	46 CFR 116.415 (a)(1)	Steel or other equivalent material
Small Passenger Vessel <150 Passengers	46 CFR 177.10-5 (A)	Minimize fire hazards insofar as reasonable and practicable
Oceanographic	45 CFR 190.07-10 (a)	Steel or other suitable material having in mind the risk of fire

Following the passive fire protection philosophy discussed previously, the US regulations generally require the hull, structural bulk heads, decks, and deckhouses to be constructed of steel unless an arrangement of other materials can be shown to perform equivalent to steel. This is illustrated in Table 1 which contains excerpts from the Code of Federal Regulations (CFR). It is clearly the intent of the regulations that ships, with the exception of smaller vessels, be constructed from materials that are non-combustible and tolerant of high temperatures.

Internationally, the SOLAS rules have, in the past, permitted construction with combustible materials if an automatic sprinkler system was installed. Recognizing the need for light weight, high speed ferry type craft, the international community has developed the International Code for Safety of High Speed (HSC Code). The HSC Code allows the use of combustible construction but only when the material meet very strict definitions (discussed elsewhere) for *fire-restricting materials* and that can be used to construct *fire-restricting divisions*. Aluminum alloys are clearly allowed. This flexibility is allowed because the HSC Code requires the vessels to meet very strict operating, management and evacuation requirements. The tests required for materials to be classified as *fire-restricting* or *fire-resisting* are very difficult for advanced materials such as composites to meet without insulating coatings. As part of past, and ongoing, MARITECH sponsored research the current team has developed a truly unique, cost and performance based approach to meet the requirements as set forth in IMO/HSC. This report is concerned with the development of a quantitative methodology to design and assess the structural fire integrity of composite ship structures.

1.3 Future Regulatory Directions

Today, the development of advanced aluminum alloy or hybrid alloy/FRP composite material systems demonstrating high performance, lower cost construction, and reduced maintenance, demands that regulations developed in the past restricting the use of novel materials, be reexamined and altered in light of current technology. *Indeed, the world community appears ready and willing to accommodate new materials provided that a thorough and technically sound analysis is completed that ensures the current level of safety is maintained.* Excerpts from the preamble of the HSC Code are evidence of this in stating for instance, that “the traditional method of regulating ships should not be accepted as being the only possible way of providing an appropriate level of safety, nor should it be assumed that another approach, using different criteria, could not be applied. Management of risk through accommodation, arrangement, active safety systems, restricted operations, quality management, and human factors engineering should be considered in evaluating safety equivalent to current conventions. Application of mathematical analysis should be encouraged to assess risk and determine the validity of safety measures.”

The past, and ongoing, work conducted at UCSD, in collaboration with the regulatory community has led to several vital new developments in structural fire protection material systems. First has been our work, conducted in collaboration with the US Coast Guard, on design for structural fire integrity; this work is intended to lead to changes in international acceptance criteria. Secondly has been our work, conducted in collaboration with a very broad section of the international materials industry as well as regulatory community, that has led to truly unique materials systems that offer both *fire restricting* performance and *fire resisting division* performance. As noted below, these systems possess the necessary characteristics including, *inter alia*, being low cost, being totally compatible with construction process, being highly durable, and being lightweight. This project was intended to develop implement these methods to further the use of advanced hybrid FRP composite materials in marine construction by the focused evaluation of new material systems and by developing new materials and analytical methods which will allow the competitive use of advanced materials in both HSC Code vessel construction and traditional SOLAS vessel construction as discussed below. The methodology developed includes affordable test methods coupled to the analytical framework.

1.4 Basic Objectives and Procedures

The basic objectives of the research conducted herein were:

1. To develop and design standards of the fire protection of structural polymer matrix composite divisions (both single skin and cored structures) in ships, based on research conducted under a DARPA MARITECH grant entitled "Internationally Competitive Fast Ferries and Composite Ship Technologies." The standard should serve as a working tool in the fire protection design methodology currently being developed under the MARITECH grant.
2. To conduct testing and research to determine the applicability of the MARITECH design methodology to composite constructions manufactured by processes other than SCRIMP; and
3. To adapt or modify the MARITECH design methodology as well as the standard to be developed as part of (1) as necessary for use with other common manufacturing processes that produce lower volume fiber-to-matrix ratios than does the technologically advanced SCRIMP process.

The procedures to be used included:

1. The Contractor's formulation of a user friendly standard for qualifying and designing polymer matrix composite structures based on previous and ongoing research conducted through the DARPA MARITECH program "Internationally Competitive Fast Ferries and Composite Ship Technologies."
2. The Contractor's exploration of the applicability of the MARITECH work to traditional composite fabrication techniques (other than the SCRIMP process) and adapt the methodology and standard as necessary to accommodate these traditional constructions.
3. The Contractor's development of the scope of any follow-on research needed to define or better design standard developed through this initiative.

2 Description of Materials and Thermal Properties

2.1 Material Descriptions

The specific composite skin materials to be described herein are composed of E-glass fabrics embedded in vinylester resins; core materials included balsa and PVC foams. Similar methods could be used to study and quantify the performance of composites made from other resin or fabric systems. The composite skins were fabricated using both vacuum assisted resin transfer molding process (*viz* SCRIMP, [4]) which produces composites with a 52 to 55 volume percent fiber-to-matrix ration, and hand-layup methods. The latter method produces fiber volume fractions on the order of 45 percent. These materials are referred to, herein, as *high-or low-fiber density* materials, respectfully. The mechanical properties of these materials have been studied including, *inter alia*, stiffness and strength before and after thermal degradation [5]. The analyses and procedures developed herein are specifically performed for materials with fiber densities in this range regardless of processing methods.

As just noted, both *in-situ* and residual mechanical properties were measured for both high and low-fiber density materials. In the case of the residual properties, mechanical response was documented at ambient temperatures *e.g.* 20⁰C after exposure to elevated temperatures for various times. The methodology developed herein, however, pertains to the *in-situ* thermal-mechanical response of the composite materials, *i.e.* at elevated temperatures.

As the data will show, thermal properties of FRP composites are inherently time and temperature dependent. Thus what are referred to as *in-situ* temperature dependent properties are actually those (degraded) properties displayed after thermal exposure times on the order of 20 to 30 minutes. More will be said about this later.

2.2 Thermal Properties of High-Fiber Density Materials and a Master Degradation Curve

Figure 1a illustrates a simple degradation law describing the reduction in properties with temperature of the skin materials prepared using the SCRIMP method. The discrete data points represent the measured loss in flexural and tensile stiffness of a 24 oz woven roving E-glass/vinylester composite [6]. As the curve indicates, most structural properties are lost as temperatures approach 130⁰C, mostly due to loss in resin stiffness. Our intention is to develop more detailed models for normalized affected composites based on out ongoing materials tests [5]. For now we use the normalized curve shown in Figure 1a to describe the temperature dependent degradation in all basic mechanical properties.

The material degradation represented by Figure 1a is meant to be the *in-situ* decrease in stiffness and strength properties at the temperatures in question. This data was obtained, in part, from Interplastics, Inc. [6] as well as the testing performed at UCSD. Similar material degradation curves can be constructed for core materials; examples for PVC foams and balsa core materials are shown in Figures 1b and 1c. Note that these curves do not represent *residual properties*, that is, those that would be displayed after a return to ambient temperature after exposure to elevated temperatures for various times. The *in-situ* properties are those displayed after times of 20 to 30 minutes of exposure to elevated temperature. Such exposure times are often necessary to assure thermal equilibrium. Residual behavior would be treated in a manner similar to what is described below, but with full account taken of the time and temperature behavior. Figure 1d shows particular set of residual property for compressive and short beam shear behavior. The data illustrates that such vinylester/glass composite systems tend to recover a large fraction of their compressive and short beam shear properties when subjected to temperatures below about 325⁰C. We note, however, that this data is for composite skin laminates that were subject to elevated temperatures without the concurrent application of stress. *Fiber composite materials subject to combined elevated temperature and mechanical loading can undergo more severe residual degradation due to misalignment of fibers at elevated temperatures.*

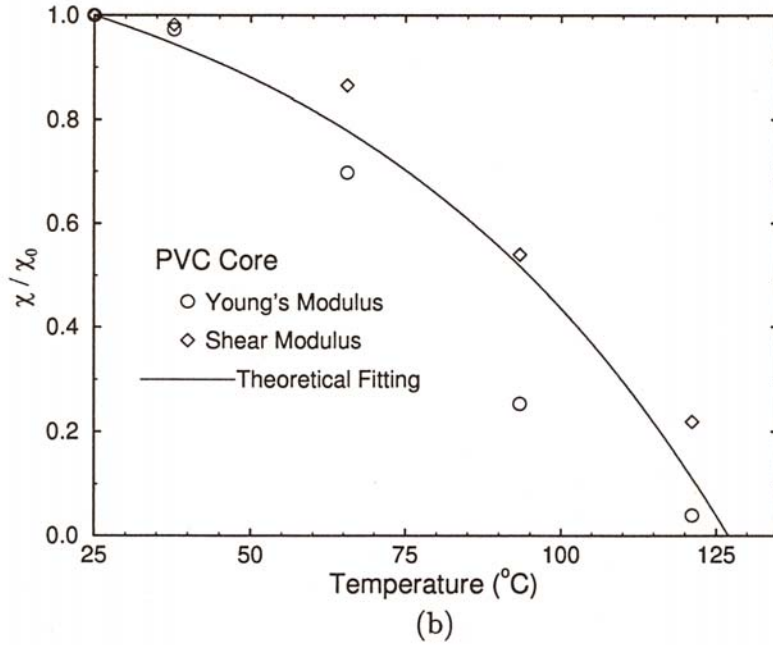
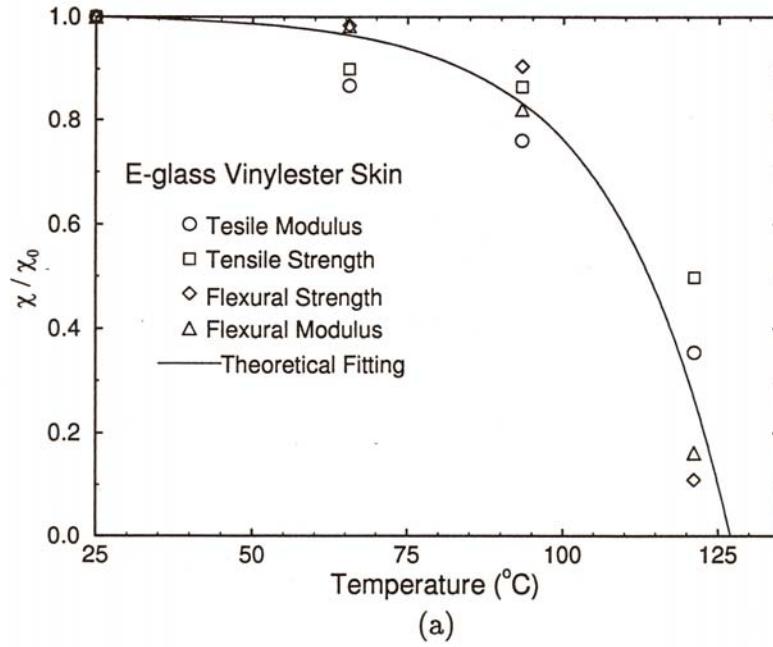


Figure 1: Property degradation curves for (a) E-glass vinylester skin material, (b) PVC core material, and (c) balsa core material; χ and χ_0 represent properties such as stiffness or interlaminar shear strength as they depend on temperature and their initial state respectively. (d) shows the residual property degradation data for E-glass vinylester skin material.

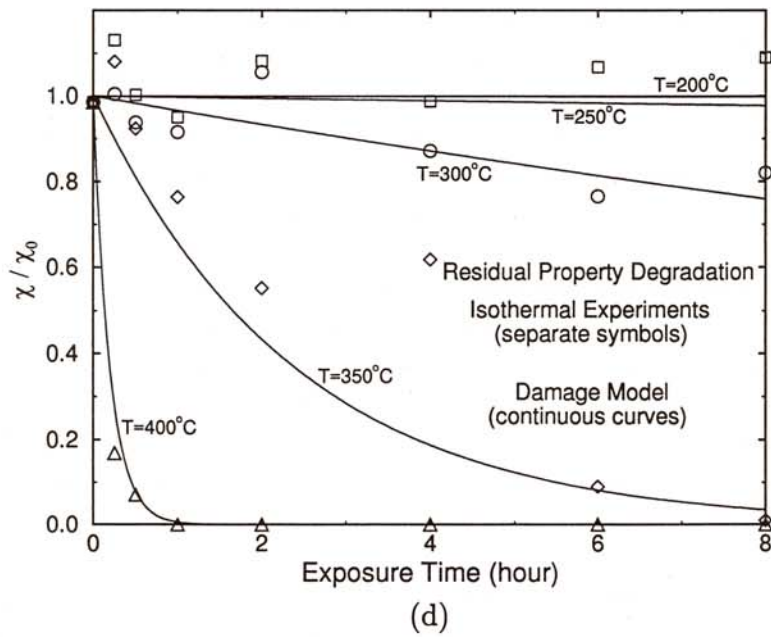
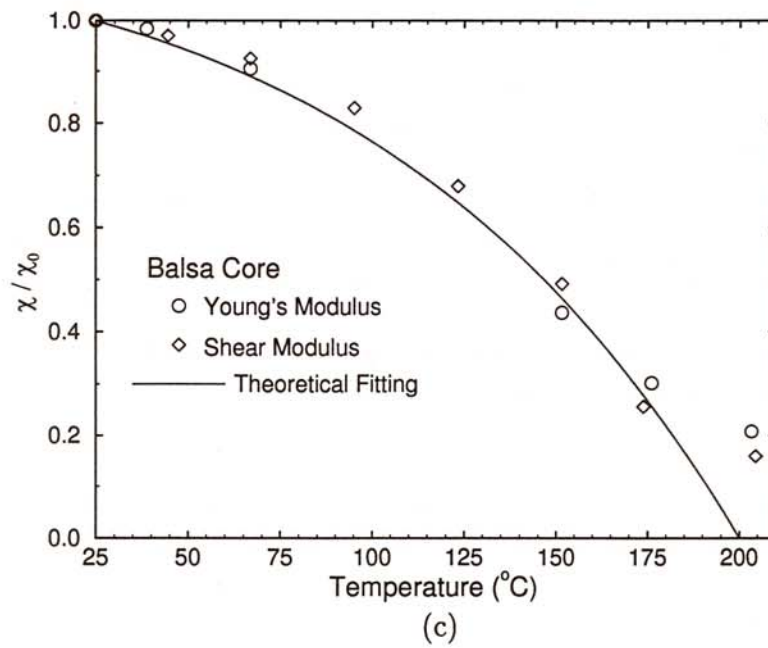


Figure 1. (cont.)

Previous studies have employed, for single skin materials only, a more semi-empirical approach to describing failure under combined thermal-mechanical loads [7, 8, 9]. The approach has been based on the notion of *failure surfaces* which are essentially plots of the time-to-failure of simply loaded panels versus the applied uniaxial stress (normalized with respect to an ambient temperature failure stress) and the incident heat flux. Data was obtained on the temperature dependence of basic mechanical properties such as tensile stiffness and strength along with shear strength. This data indicates degradation behavior similar to that shown in Figure 1a. The approach, based on empirically determined failure surfaces as defined above, does not constitute a true material constitutive theory although the temperature dependent stiffness data would be useful as input to calibrate such a constitutive framework. This approach taken here involves the development of a quantitative constitutive framework which is then used to analyze full structural response under arbitrary thermo-mechanical loadings.

2.3 Thermal Properties of High-and-Low-Fiber Density Materials

2.3.1 Material and Test Methodology

In order to assess material performance under elevated temperature conditions, a test program was undertaken to characterize material response under tension, compression or flexural loading. Response was measured through testing a minimum of three specimens under two different testing conditions: (a) after exposure for a specified time period and cool-down so as to assess residual performance, and (b) at temperature after exposure for a specified time.

A number of materials using different combination of E-glass fabric and resin were processed using either the wet layup process using a vacuum bag, or through the use of SCRIMP. Panels were supplied by fabricators without post-cure. Specimens were cut to the required test dimensions (*per* type of test to be conducted) and were conditioned by placing them in a humidity chamber at 50-55 percent RH for 30 days prior to testing. Each coupon was weighed prior to exposure and coupons used for residual performance testing were also weighed after exposure to assess weight loss. Specimens were exposed to elevated temperatures using an oven. In the case of specimens tested at temperature, specimens were first heated in the oven and then brought out in a "hot" box enclosure around the test specimen and fixture. It is likely that some heat was lost in the transfer process prior to testing using this procedure.

2.3.2 Material Test Results and Discussions

A total of 15 different material sets were tested under this program, of which a few examples are described below. It should be noted that fiber weight fractions varied from one set to the next based on the process and fabric architecture used. However all specimens using SCRIMP process show a fairly uniform loading of 50-55 volume fraction, with the exception of specialized fabrics (such as *needle-punched* specimens).

Figure 2 and 3 depict levels of normalized tensile strength obtained from testing after exposure and cool-down, and at temperature respectively, for composites fabricated from 2 layers of a quadriaxial nonwoven QM5708 impregnated with a Corezyn Vinylester using the wet layup process and vacuum bagging. The specimens had a fiber weight fraction of 62 percent and were tested after exposure to temperatures ranging from 100 to 325⁰C. As can be seen, there is a dramatic drop in strength when tested at temperature compared to the changes in residual properties. The changes seen in values above initial conditions (23⁰C) can be contributed to effects of post-cure and are generally seen after short-period exposures.

Figures 4 and 5 depict a similar trend in the VEX1559-540 specimens using SCRIMP. It should be noted that these specimens had a comparatively lower fiber loading of 50 percent weight fraction due to the special fabric construction. Comparison of the trends in Figures 4 and 2 show a greater effect of post cure in the VEX specimens due to the greater resin content. However, this also causes a sharper and greater drop in properties as seen at levels of 300 and 325⁰C in Figure 4 and in Figure 5, where the overall reduction in properties at temperatures higher than 150⁰C is substantially greater.

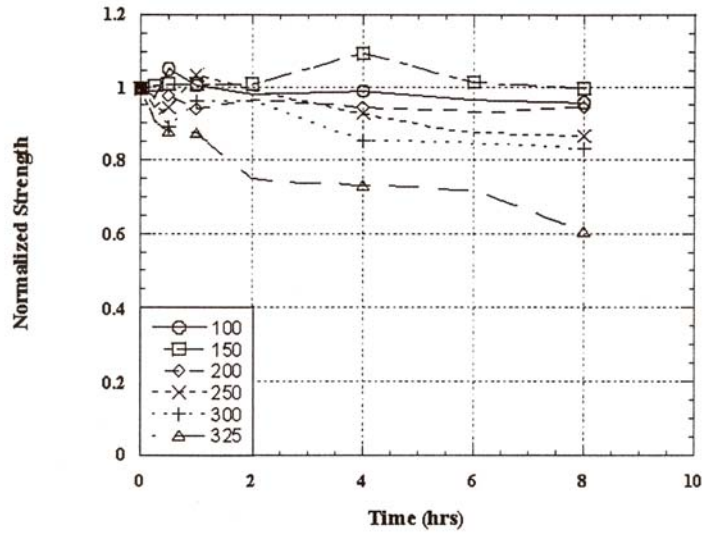


Figure 2: Residual normalized tensile strength for composite fabricated from 2 quadriaxial nonwoven QM5708 impregnated with Corezyn Vinylester using wet layup process and vacuum bagging.

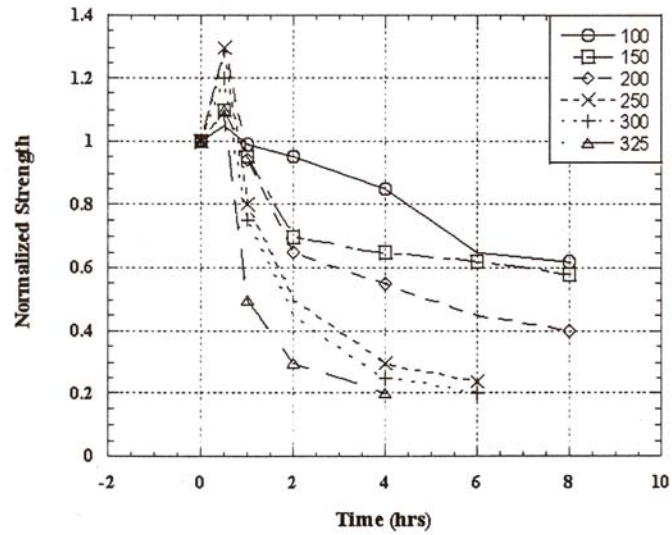


Figure 3: Normalized tensile strength from testing at temperature for composite fabricated from 2 quadriaxial nonwoven QM5708 impregnated with Corezyn Vinylester using wet layup process and vacuum bagging.

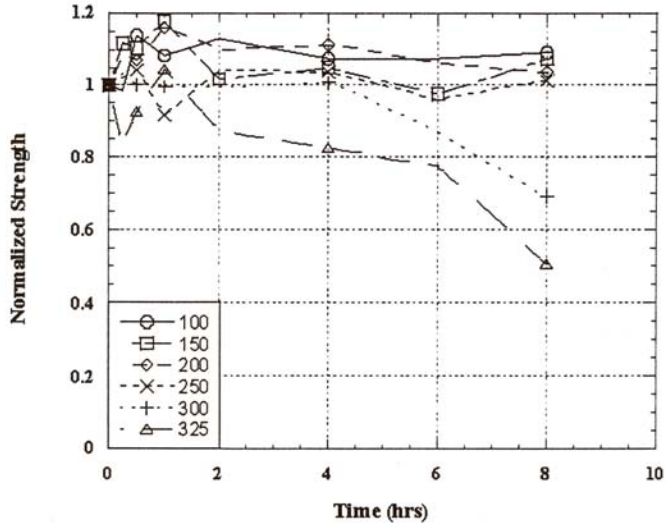


Figure 4: Residual normalized tensile strength for VEX159-540 specimen fabricated using SCRIMP.

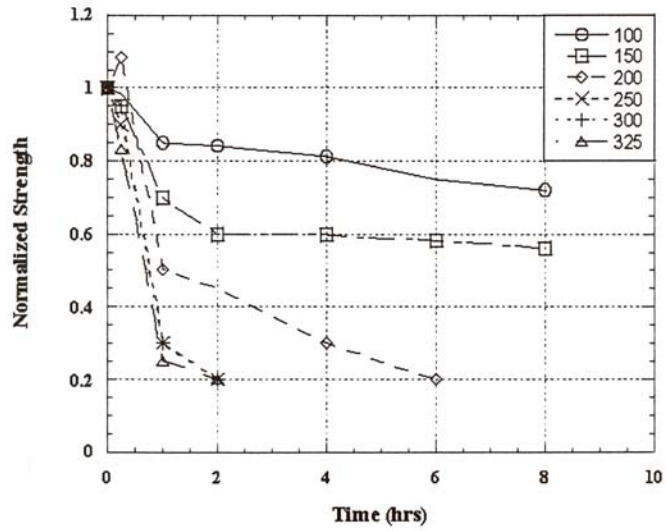


Figure 5: Normalized tensile strength from testing at temperature for VEX159-540 specimen fabricated using SCRIMP.

A major concern with the use of layered composites is the dependence on resin integrity between layers. Although the effect of interlaminar layer integrity is not seen as clearly in tensile test as it would be in flexure or short-beam-shear, the effects are clearly apparent at higher temperatures ($> 300^{\circ}C$) wherein the thickness of the coupon is seen to increase due to the lack of resin causing of the fabric structure after exposure to elevated temperatures. The use of *needle-punching* is viewed as a cost-effective means of increasing through thickness integrity without having to resort to expensive stitching or weaving methods. Figure 6 and 7 compare the effects of testing of specimens, fabricated using the SCRIMP method, with a 0.42 weight fraction loading, after heat and cool-down with those of testing at temperature. It can be seen that there is a discernible effect of the through thickness reinforcement on performance at elevated temperatures, although temperatures about $300^{\circ}C$ still result in a significant degradation of performance.

Since the tension test intrinsically grips fiber ends, it can be expected that even at relatively high levels of resin (and hence composite) degradation due to heat there will be a certain degree of stress translation along the fiber itself. Structural components in marine structures have to bear compressive loads as well, and hence it is of interest to assess effects on compressive properties since the degradation of resin would intrinsically cause collapse of the microstructure through shearing of fiber bundles under load in addition to out-of-plane deformation and buckling. Figures 8 and 9 depict the effects of testing after exposure to varying period of temperature in tension and compression, respectively, for a Woven roving-chopped mat configuration fabricated using SCRIMP. It can easily be seen that the effects are substantially greater under compressive loads. It should be noted that DCS characterization of the material indicated that the composite was received with only 83-88 percent cure and hence the lower temperature exposures could be reasonably expected to increase cure and hence performance through post-cure.

In order to increase damage tolerance and impact resistance, resins are often toughened through additives and changes in formulation. Although this has been shown to be modestly effective, the use of toughening agents also leads to an increase in viscosity of the resin system, making it more difficult to use in SCRIMP. Figures 10 and 11 show results of residual normalized tensile and compressive strengths, respectively, of specimens fabricated using XM fabric and CIBA resin using SCRIMP. Overall, the trends show sharper degradation in performance when compared with the corresponding results in Figures 10 and 11. It should be noted, however, that the former set used a woven fabric tested along the warp direction, whereas the latter set used an angle-bias fabric.

Increase resistance to elevated temperatures and fire can be achieved through the use of specially formulated resin system. Figures 12 and 13 show the results of normalized residual tensile and compressive strengths, respectively, using a specially formulated fire resistant resin in a composite fabricated using the wet layup process, whereas, Figures 14 and 15 depict effects of temperature and time of exposure on flexural strength performance for tests conducted after cool-down, and at room temperatures, respectively.

A comparison of Figure 5 and 7 with Figure 15, illustrates the difference in *in-situ* temperature dependence of strength between high- and low-fiber density materials. Hand laid-up low-fiber density materials lost most, or all, of their effective strength after even relatively short time exposures to temperatures in the range of 100 to $150^{\circ}C$. Such is not the case for high-fiber density materials.

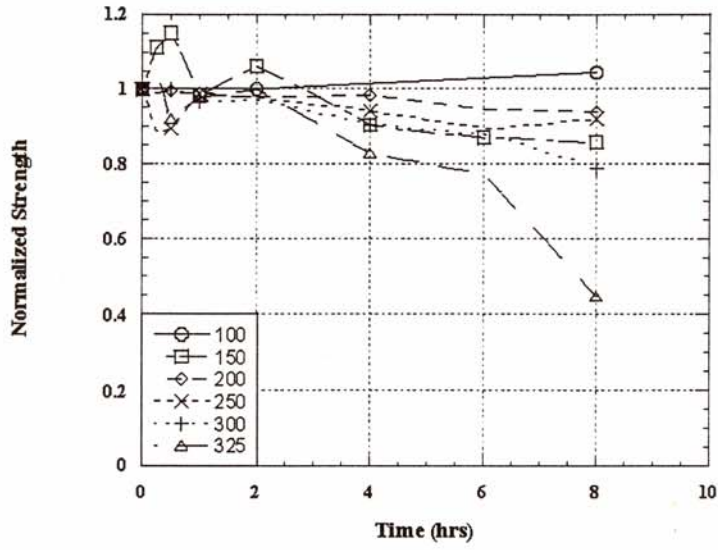


Figure 6: Residual normalized tensile strength for needle-punched specimen fabricated using SCRIMP.

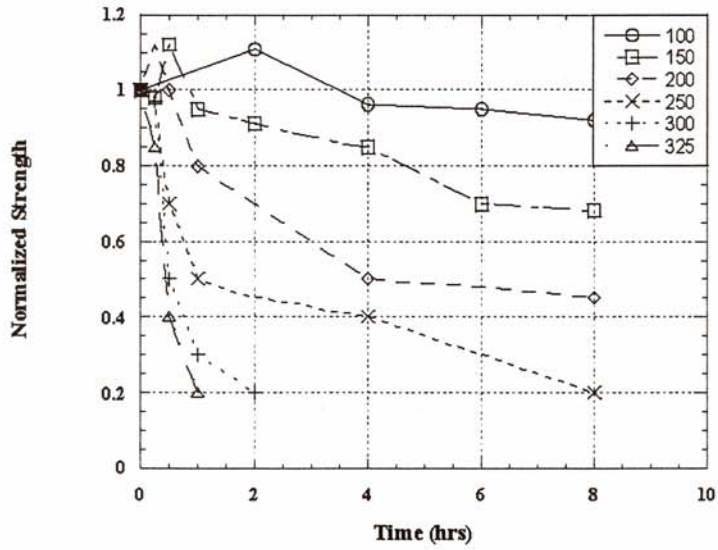


Figure 7: Normalized tensile strength from testing at temperature for needle-punched specimen fabricated using SCRIMP.

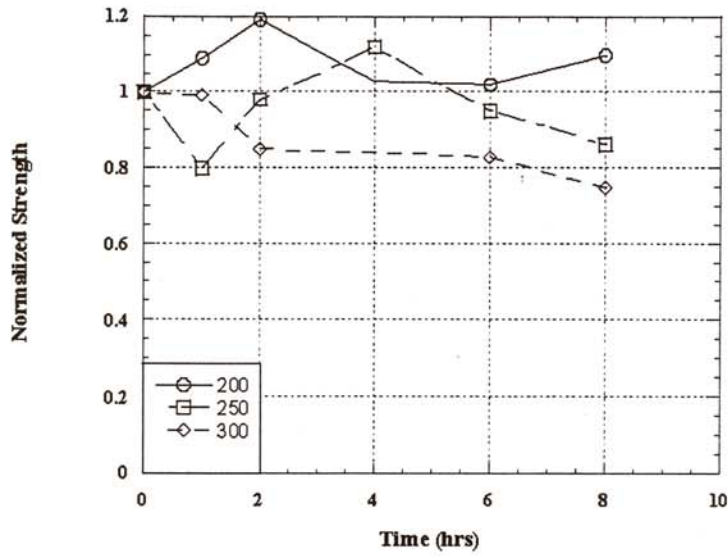


Figure 8: Residual normalized tensile strength for a Woven roving-chopped strand mat configuration fabricated using SCRIMP.

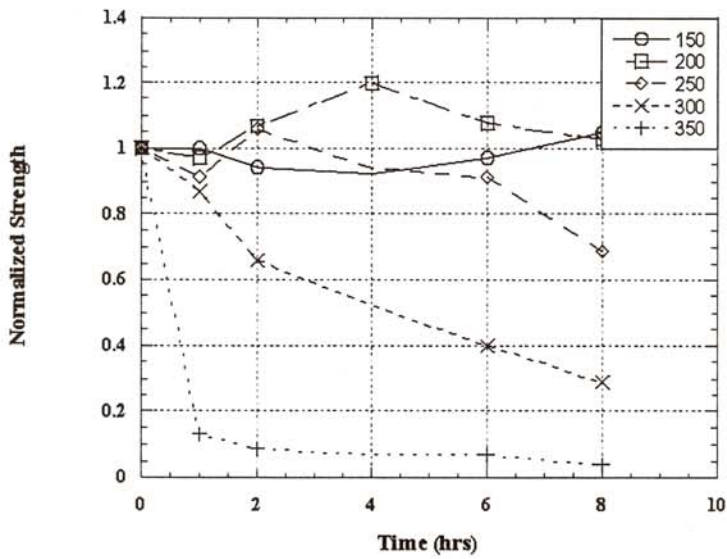


Figure 9: Residual normalized compressive strength for a Woven roving-chopped strand mat configuration fabricated using SCRIMP.

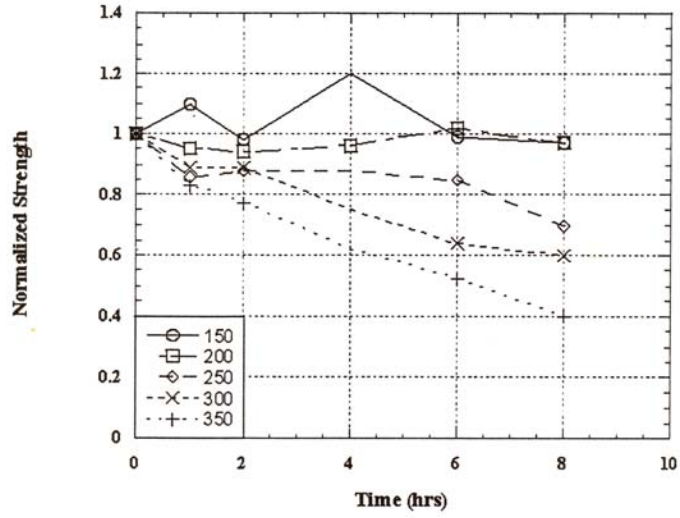


Figure 10: Residual normalized tensile strength for XM fabric and CIBA resin fabricated using SCRIMP.

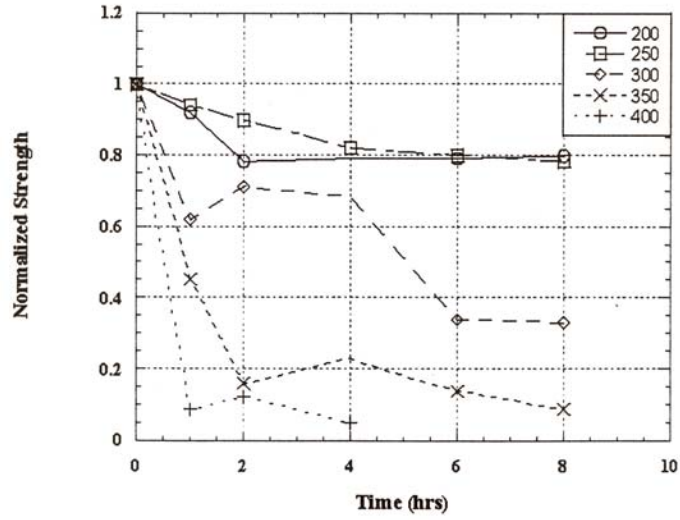


Figure 11: Residual normalized compressive strength for XM fabric and CIBA resin fabricated using SCRIMP.

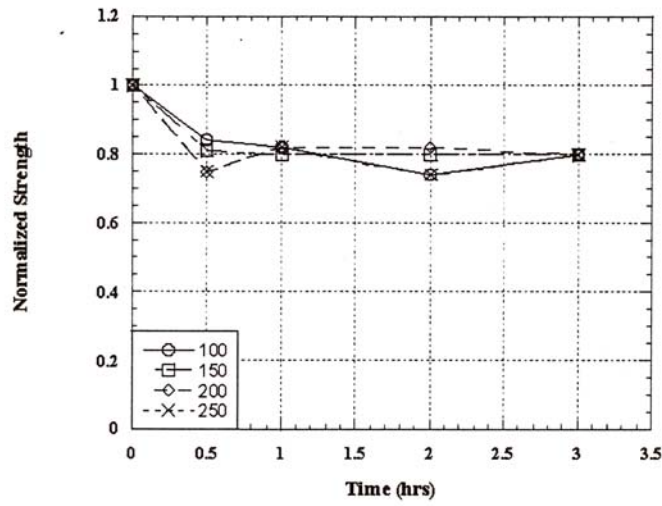


Figure 12: Residual normalized tensile strength for a specially formulated fire-resistant resin fabricated with wet layup process.

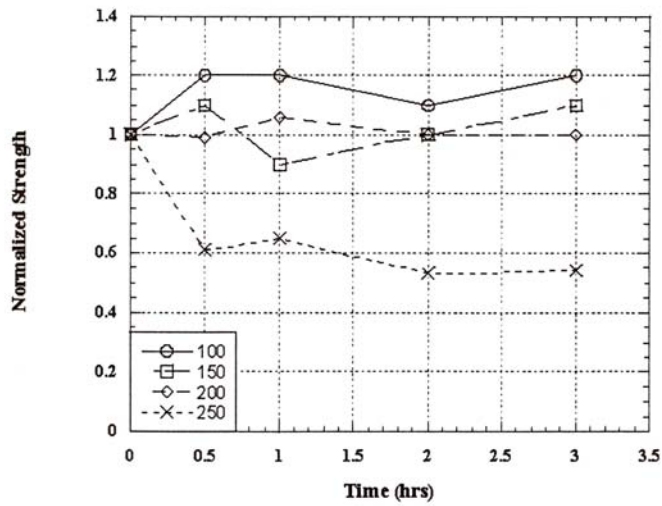


Figure 13: Residual normalized compressive strength for a specially formulated fire-resistant resin fabricated with wet layup process.

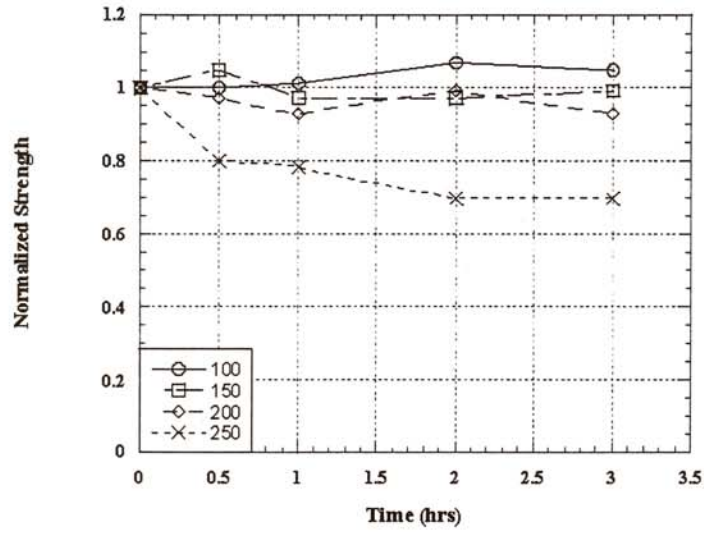


Figure 14: Residual normalized flexural strength for a specially formulated fire-resistant resin fabricated with wet layup process.

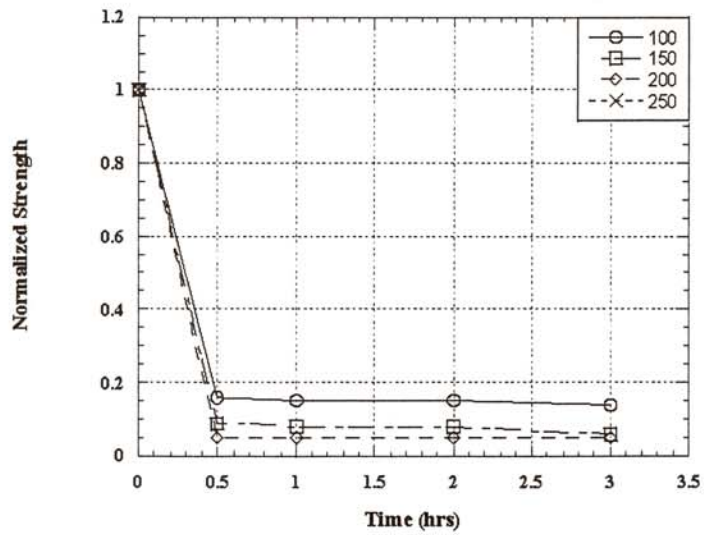


Figure 15: Normalized flexural strength from testing at temperature for a specially formulated fire-resistant resin fabricated with wet layup process.

3 Standards for Alloy Construction and Overall Approach

Construction with aluminum alloys generally requires that insulation prevent the "core" temperatures from exceeding $200^{\circ}C$ for the required fire protection time [10]. For perspective, it is useful to attempt to establish a rational basis for such a criteria. To this end, the boundary value problem for an ideal aluminum alloy panel (with rectangular cross section) subject to uniaxial compressive load was solved. The aluminum alloy panel has the geometry $l \times w \times h$ (length x width x thickness; ($w \gg h$), and is pinned at both ends. The tangent modulus method of Shanley [11] is used to calculate the elastic-plastic collapse load expressed as a compressive stress $load/wh$. Figure 16 shows the temperature dependent variation of yield ultimate tensile strengths of a 6061 aluminum alloy used for one particular analysis. Figure 17 shows the resulting variations of critical collapse stress, *i.e.* 'collapse load' averaged over the area of the panel cross-section $P_{coll}/(wh)$. It is obvious that, due to the degradation of strength with temperature, the collapse loads fall rapidly with increasing temperature.

To establish a safety criterion, horizontal lines have been drawn at the levels of 0.5 and 0.67 with the following perspective: original design safety factors of 2 or 1.5 would mean that if the collapse stress would fall below factors of 0.5 or 0.67 of the initial collapse stresses, respectively, all structural safety would be lost as indicated in Figure 17. The temperatures at which this occurs thereby establishes threshold temperatures above which (for short times at temperature, and neglecting creep deformations) structural integrity is lost.

Insulation and fire extinguishing requirements are therefore prescribed, and mandated, to prevent exceeding these temperatures for the required fire protection times. The fact that the temperature range found from Figure 17 is $166^{\circ}C \leq T \leq 192^{\circ}C$ helps explain how a $150 - 200^{\circ}C$ temperature limit may be established for aluminum alloy design. The specification of keeping aluminum core temperatures below $200^{\circ}C$, in turn, prescribes the performance requirements of the coatings and/or insulation used for fire protection.

The analysis just described is consistent with the approach outlined in Figure 18, although the analysis for aluminum alloys would not in itself require such an elaborate description. The process of establishing 'allowable' incident heat fluxes and skin or core temperatures is itself explained in the figure. The approach begins with a characterization of imposed heat fluxes and temperatures that are anticipated in shipboard fires. Material properties must likewise be characterized in temperature ranges that are anticipated to result from such thermal exposures. The loss in structural integrity, *e.g.* the loss in load bearing capacity, must be then characterized. When the losses in load bearing capacity are evaluated *vis-a-vis* then appropriate design criteria, including the factors of safety used, limits would then be set for the tolerable thermal exposure. In the case of aluminum alloys, tolerable exposures are those that do not lead to temperatures in excess of $200^{\circ}C$ within the quoted fire protection time. According to Figure 17, this temperature would be based on the use of a factor of safety of 2. For composites, however, the process of establishing allowable thermal loads, and thus for establishing required fire protection levels is more complex as discussed next. What is also worth noting is that constitutive theories for alloys exist so that, if temperature dependent constitutive data were known, complete structural analyses would be possible. A similar quantitative methodology is needed for FRP composites.

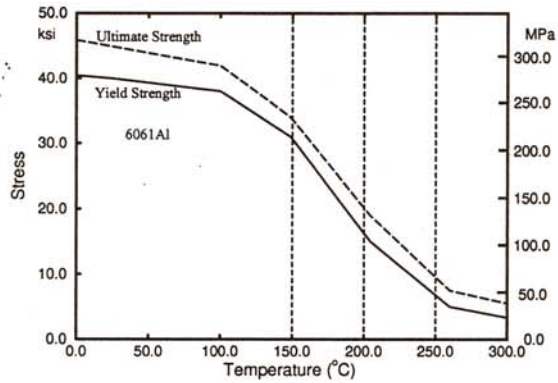


Figure 16: Temperature dependent variation of yield and ultimate tensile strengths for elastic-plastic buckling analysis of 6061 aluminum alloy panels.

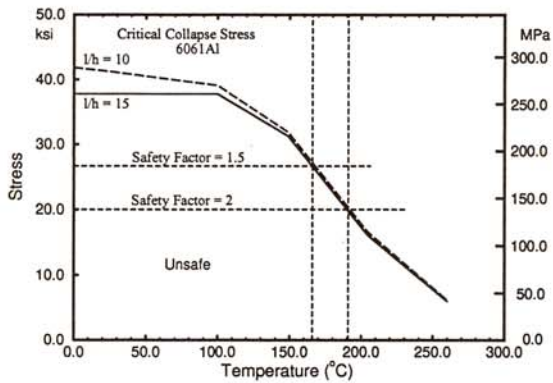


Figure 17: Variations of critical collapse stress, *i.e.* "collapse load" averaged over the area of the panel cross-section $P_{coll}/(wh)$ for elastic-plastic buckling analysis of 6061 aluminum alloy panels.

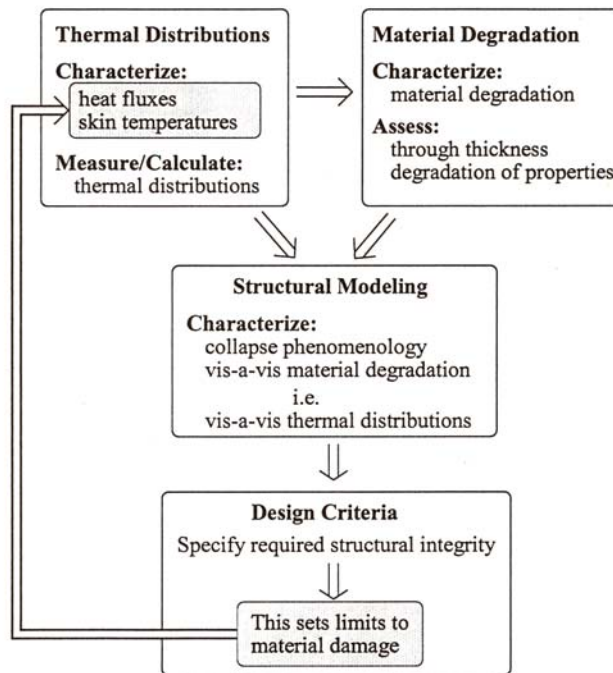


Figure 18: Modeling approach.

4 Failure Modes and Mechanisms in FRP Composites

The structural analysis of the failure of aluminum alloys is less difficult than with composites due to 1) reasonably assumed isothermal conditions within aluminum sections, and 2) the relative simplicity of the failure mode, *viz* uniform thermal degradation of stiffness and strength. There is no assumed, or anticipated, change in failure mode due to elevated temperatures in the case of alloys. Composite materials, on the other hand, possess much lower thermal conductivities (especially in the through thickness direction). They develop temperature gradients and thereby gradients in stiffness, strength, and physical properties. The analysis of structural failure and the bases for setting allowable limits for thermal loading are, accordingly, more difficult. Still another reason for the increased difficulty in conducting structural analyses of composites is that the failure modes are more varied and complex than in aluminum alloys. This is illustrated in Figure 19. This figure describes three basic compressive material and structural failure processes due to the more rapid decrease in resin properties with increasing temperature as compared to fiber properties. This results in the loss in fiber confinement and a decrease in interlaminar shear strength this, in turn, leads to a reduction in the critical stresses for kinking, buckling, and wrinkling. In tension tests, the load is mainly supported by fibers whose properties are less sensitive to modest temperature elevations.

As just noted, compressive failure modes indicated in Figure 19 are sensitive to resin properties. Kinking, or microbuckling, is a compressive material failure mechanism. In a single skin composite it may be a precursor to global buckling or to fiber failure. As illustrated in Figure 19, σ_{crit} , the critical stress required to cause such failures is strongly dominated by the composite's interlaminar shear strength which, as noted, is strongly temperature dependent. Reductions in τ_y , the interlaminar shear strength, caused by resin softening will thereby tend to promote microbuckling. Skin wrinkling, as illustrated in Figure 19, is a failure mode in cored, *i.e.* sandwich composites, that can lead to delamination. The criteria demonstrates a sensitivity to the moduli of both the skin and core materials, both of whose values will degrade with temperature. The variational formula shown below for σ_{crit} indicates that variations (*e.g.* decreases due to increased temperature) in core properties can lead to proportionally larger reductions in σ_{crit} than do reductions in skin stiffness. Similar comments can be made with respect to structural buckling as illustrated by the equations shown in Figure 19.

The strong temperature gradients that develop in either single skin, or cored, composites lead to degradation in the stiffness and strength properties of the composite skins and cores. Examples of thermal gradients are shown later. The extent of these reductions in properties will be depend on the detailed manner in which the skin and core material properties change with temperature and the temperature distributions. Which failure mode limits structural integrity will depend on these details and thus it is possible that a change in failure process could accompany a change in the temperature field. Of course, geometry plays, under all conditions, a vital role. For very slender panels under compression, structural buckling can easily dominate the failure; this, in fact, seems the case for the panel failures discussed later in Section 6. In particular, for panels with height to width ratio's greater than 20, structural buckling appears to dominate in undamaged and damaged conditions.

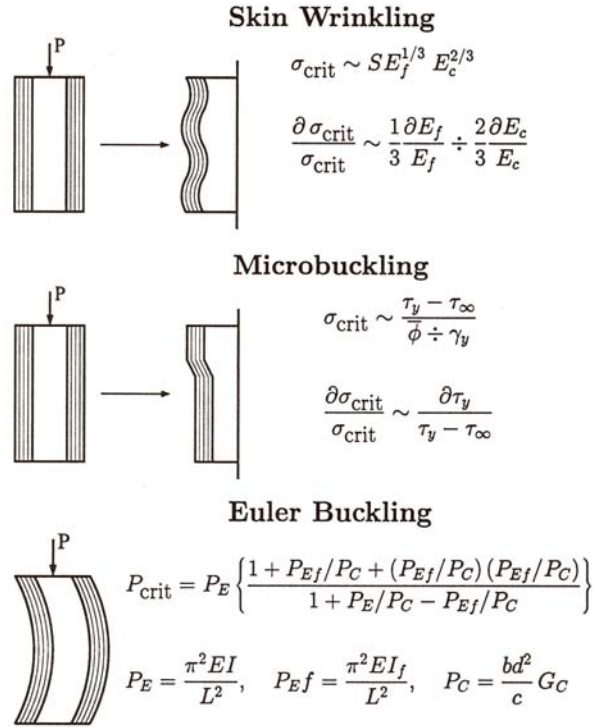


Figure 19: Failure mechanisms in composites. E_f and E_c are sandwich “face” and “core” stiffness respectively. τ_y is the interlaminar shear strength and τ_∞ the remotely applied shear stress. G_c is the in-plane shear stiffness of the “core” material, and E is again the “face” stiffness. $\bar{\phi}$ represents an imperfection in the fiber layup and is the (assumed small) angle of initial misorientation of axial fiber with the composite axis.

5 Experimental Procedures for Testing Panels Under Compressive Loading

Panels were subjected to incident time-temperature histories that followed the E-119 temperature protocol. It is noted that this temperature-time history is similar to that prescribed by IMO Resolution A.754 (18) *vis-a-vis* the testing of *fire resisting divisions*. Figure 20 illustrates the multi-axial loading apparatus that was used to apply combinations of in-plane loads and out-of-plane loads. Two hydraulic rams were located on the top edge controlled in-plane loads, or displacements, and a single ram located on the unexposed side, applied out-of-plane load or displacements. Out-of-plane (or displacements) may be applied in either directions, *i.e.* the panels may be deflected into or away from, the flame. The fixture is bolted down onto the rim of a furnace for fire exposure. Displacements are measured on the top edge and along the out-of-plane ram.

Although the panels are fixed into slotted rods at the top and bottom of the test fixtures, the boundary conditions at the top and bottom edges are not taken as *rigid*. Observations indicated that there end were nearly free rotation, *i.e.* *pinned*. Analysis were conducted using both rigid and pinned type boundary conditions and it was found that the latter produced results that most closely matched the test results.

As noted above, two types of materials were included in our study, *viz* high- and low-fiber density materials. Their architectures are as described below:

5.1 High-Fiber Density Panel Architecture

Single skin panels were nominally 0.48in (12.2mm) thick, 36in (914.4mm) long and 28in (711.2mm) wide. They were nominally composed of a 56oz, 5608–08 Quadraxial E-glass fabric, vacuum infused, *via* *SCRIMP*TM in a VEX vinylester matrix; as noted earlier, the fiber density was approximately 55 percent by volume. The insulation used was a two-layer 8lbs mineral wool; this represents two, nominally 1in (25.4mm) thick, panels of insulation on the fire side. This insulation was used to control the heat fluxes imposed on the FRP composite panels. Looking ahead to Figures 22 and 25, the thermal loading and fire insulation produced the exposed face temperatures as shown. It can be noted that such insulation provided excellent protection *vis-a-vis* the E-119 fire loading. Panels so protected were observed to support loads of up to 5,000lbs (22.24kN) during the tests for up to 60 minutes.

In some single skin panels, thermocouples were placed at three locations through the thickness and at various locations on the panels' in-plane area. These interior thermocouples were co-molded in during panel fabrication. In all panels, thermocouples were mounted on the fire exposed, and unexposed, faces at several locations on the in-plane area. The interior thermocouples served to calibrate our thermal analyses and established accurate estimates for thermal conductivities. *As noted, once thorough thermal characterization of the panels was done, interior thermal couples were not used.*

The procedure for testing sandwich panels was similar. The sandwich panels were standardized to have 3.6mm (0.14in) symmetric skins and a 12.7mm (0.5in) 9lbs balsa or PVC form core. The skins were composed of two layers of the same 56oz, 5608-08 Quadraxial E-glass fabric vacuum infused *via* the SCRIMP process. In Sections 9 and 10, examples of temperature gradient profiles are shown for sandwich panels. These were measured by thermal couples placed on the exposed faces, in the center of the cores, and just behind the exposed face skin at the interface between the exposed skin and the core.

5.2 Low-Fiber Density Panel Architecture

The test method used on the low-fiber density materials was similar, but their geometries were somewhat different. For example, the single skin panels were nominally 0.44in (11.11mm) thick. Sandwich panels had skins that were 0.14in (3.56mm) thick, with 0.5in (12.7mm) thick balsa cores.

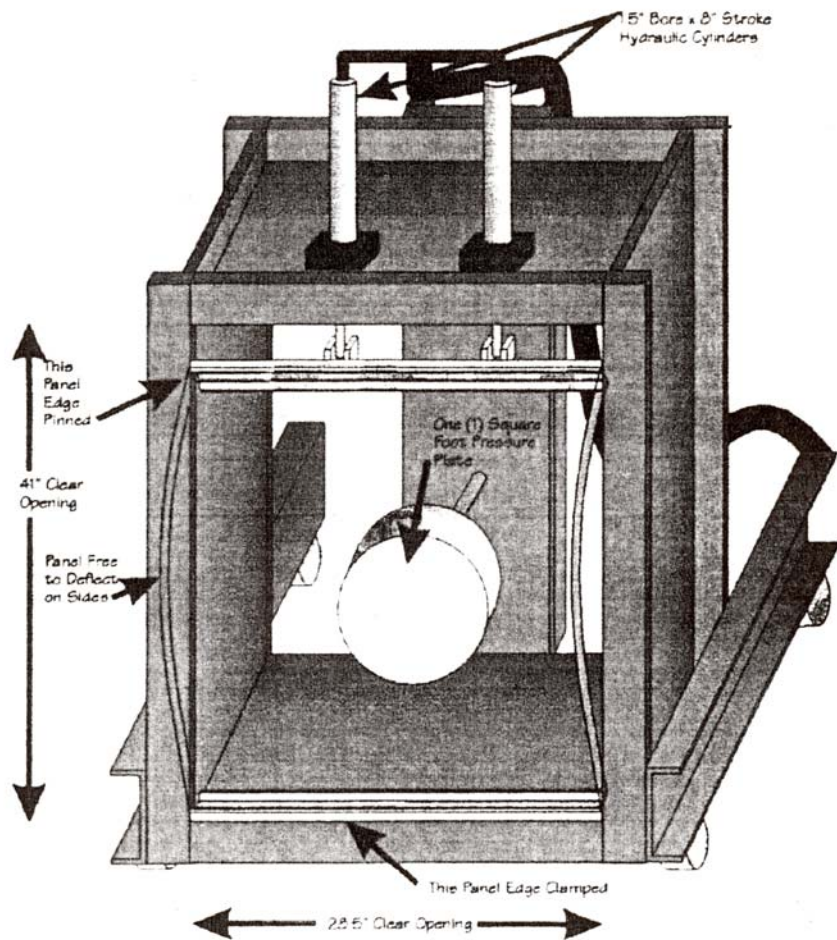


Figure 20: Multi-axial loading jig.

6 A Single Skin Model

6.1 A Simple Collapse Model

Here we present a simple model of a single skin composite that has undergone thermal damage as depicted in Figure 21. Pin supported end conditions are assumed and the panel is taken to be subject to symmetrically applied compressive loads. Recall that these boundary conditions are those that most closely matched those imposed by the loading apparatus described in Section 5 above and in connection with Figure 20. This single skin model does not account for the phenomenology of kinking, wrinkling and delamination that may occur and thus only attempts to describe macroscopic collapse *via* structural ‘buckling like’ collapse modes; cored panel failure modes will be discussed later in Section 9. The model does, however, naturally account for geometrical scaling in terms of panel dimensions

As a result of an assumed temperature gradient, and the resulting loss in material stiffness, the properties develop a corresponding gradient as indicated in the figure; here again χ represents a typical property such as stiffness or strength. The gradient in material properties is assumed to be of the general form

$$\chi = Ax^2 + Bx + C, \quad (1)$$

and with reference to Figure 21, replacing χ with Young’s Modulus E ,

$$A = (2\Delta - 4\Delta_1)/h^2, \quad B = (4\Delta_1 - \Delta)/h, \quad C = E_f\Delta_1 = E_c - E_f, \quad \Delta = E_b - E_f. \quad (2)$$

It should be noted, with emphasis, that the collapse loads computed this way depend sensitively on the gradient’s form. We also note, in passing, that if $E_c = (E_f + E_b)/2$ the gradient is linear. In the context of a thermally loaded structure, E_f would represent the ‘‘exposed face’’ property (*e.g.* modulus) and E_b the ‘‘back face’’, or ‘‘unexposed face’’ property. E_c is a property value at the panel’s center and whether it is greater, or less, than $E_f = E_b/2$ determines the shape of the gradient. Before the thermal loading begins, $E_f = E_b = E_c$; as the exposure time increased, E_f , and then eventually E_c , decrease. At longer times the back face temperature elevates and E_b then also decreases.

A simple beam theory analysis [2] shows that the collapse load, P_{coll} , can be expressed as

$$\frac{P_{coll}}{P_E} = 1 - \frac{1}{12}\Gamma^2 + \frac{2}{15}\Gamma^- \quad (3)$$

with

$$\Gamma \equiv \frac{E_b - E_f}{E_0}, \quad \Gamma^- \equiv \frac{E_b - 2E_c + E_f}{E_0}, \quad E_0 \equiv \frac{E_b + 4E_c + E_f}{6}.$$

P_E is an Euler buckling load defined as

$$P_E \equiv \frac{bh^3\pi^2}{12L^2}E_0. \quad (4)$$

Some specific cases are worth examining for perspective.

When $E_c = (E_f + E_b)/2$ the gradient is linear, $\Gamma^- = 0$, and (3) becomes

$$\frac{P_{coll}}{P_E} = 1 - \frac{1}{12}\Gamma^2, \quad (5)$$

with

$$P_E = \frac{bh^3\pi^2}{12L^2}E_0, \quad \Gamma = \frac{E_b - E_f}{E_0}, \quad E_0 = \frac{E_b + E_f}{2}.$$

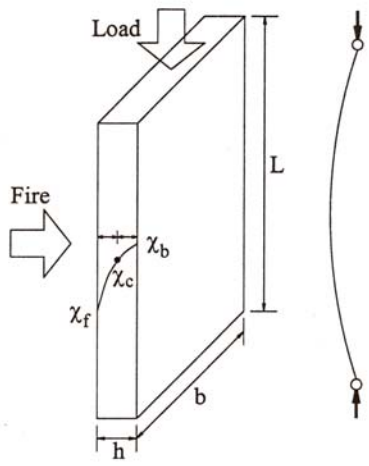
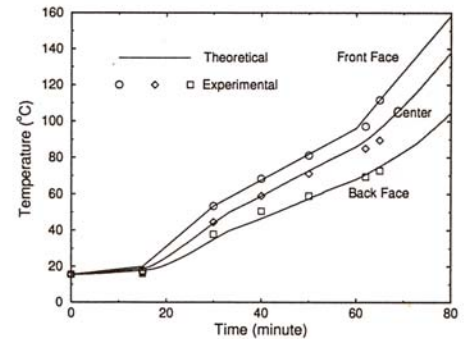
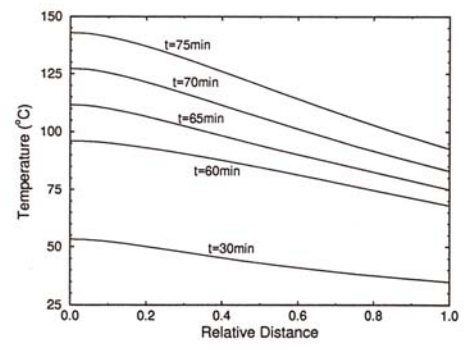


Figure 21: A simple collapse model with material property variation.



(a)



(b)

Figure 22: Thermal analysis results for Case #1: (a) temperature *versus* time plots at different panel positions, and (b) temperature distribution profiles at different fire exposure times.

In this linear case, P_E is the Euler buckling load for a "uniform companion panel" with an average of the exposed and back face moduli. When $E_f \rightarrow 0$, *i.e.* when the exposed face modulus vanishes, as temperatures at this face exceed $130^\circ C$, P_{coll} is approximately $0.66P_E$. P_E at this point is, itself $P_E = P_E^0/2$ where P_E^0 is the Euler buckling load of a uniform panel of modulus E_b . If E_b were the panel's original (*i.e.* unexposed and uniform) modulus, the damage so described would thereby lead to a collapse limit of $P_{coll} \approx 0.66(P_E^0/2) \approx P_E^0/3$. Safety factors of 3 would have been required to ensure full structural integrity in anticipation of this type of material damage. We note again that the collapse loads are sensitive to the assumed form for the property gradient; the linear gradient with $E_f \rightarrow 0$ represents a severely damaged panel. Nonetheless, the analyses show that avoiding such damage through the use of protective layers may be necessary since safety factors of 3 are often difficult to achieve in structural design.

To explore the effect of the gradient form let, for discussion's sake, $E_c = 0.75E_b$ and, again, $E_f = 0$; as shown later this corresponds more closely to observed fire damage. Now $P_{coll} = 0.475P_E^0$. As this is now approaching a condition where $P_{coll} \approx P_E^0/2$ the implication is that design safety factors of 2 would be required to ensure structural integrity. Such safety factors are more within bounds of typical design criteria.

6.2 Micromechanical Considerations

The integrated experimental/theoretical approach outlined in Section 3 is aimed at developing a quantitative methodology for assessing the structural integrity of composite materials subject to severe thermal loads caused by fire. The approach involves modelling composite material degradation due to fire loads and developing an analytical and computational methodology to describe the loss in load bearing capacity (*i.e.* structural integrity) of composite structures. Direct outputs of this specification would be the maximum thermal loads that typical structural members could tolerate for required fire protection times, along with a quantitative framework for assessing structural response during and after a fire (Figure 18). An end prescription might be a set of relatively simple design models of the type described in Section 6.1. These models would allow a quantitative assessment of the loss in load bearing capacity accompanying material damage which itself is quantitatively linked to thermal profile. It is vital, however, to insure these models do not omit critical phenomena or processes, including micromechanical ones, that may control the failures. For this reason we have performed detailed computational studies of compressive failures to compare with experimentally observed failures in our earlier study (Asaro and Dao [2]).

Detailed layered structure and the three dimensional geometry were modelled using three dimensional layered shell elements, and the three dimensional finite element analysis gave practically the same results as our simple two dimensional model presented in Section 6.1.

Also, detailed kink band analyses were performed to check the possibilities of kinking-type micromechanical failure modes. It was concluded that, unless we took unusually extreme material properties or very large initial material imperfections, the single skin panel under fire degradation would fail under the structural buckling mode. *This, in effect, leads to an additional assumption, viz. that the composite materials to be used in ship construction are of a high quality and relatively free of defects, imperfections in fiber alignment, or pre-existing debonded areas.*

With the above information in mind, we can now apply the model presented in Section 6.1 for the structural analyses in later sections.

7 Single Skin Model Analyses and Experimental Results

Detailed thermal analysis were carried out for the purpose of constructing complete temperature-time profiles from the measured thermocouple data. Results of these calculations are shown for high-fiber density materials; the results for temperature profiles in the low-fiber density panels are quite similar.

7.1 Thermal Analysis and Case 1 (High-Fiber Density Materials)

A finite difference thermal analyses code was used to simulate the temperature distributions. The code is 3-dimensional and assumes the thermal conductivities to have orthotropic symmetry. The heat conduction equation is

$$\frac{\partial}{\partial x}[k_x(T)\frac{\partial T}{\partial x}] + \frac{\partial}{\partial y}[k_y(T)\frac{\partial T}{\partial y}] + \frac{\partial}{\partial z}[k_z(T)\frac{\partial T}{\partial z}] = \rho C_p \frac{\partial T}{\partial t}. \quad (6)$$

where $k_x(T)$, $k_y(T)$ and $k_z(T)$ are the heat conductivities along x , y and z directions respectively, ρ is the density of the material, C_p is the specific heat, T is the temperature and t is the fire exposure time. Assuming a uniform in-plane temperature distribution, the problem reduces to a one-dimensional simple case, where the heat conduction equation becomes

$$\frac{\partial}{\partial x}[k_x(T)\frac{\partial T}{\partial x}] = \rho C_p \frac{\partial T}{\partial t} \quad (7)$$

The initial condition for (7) is given as

$$T(x, 0) = RT \quad (8)$$

where RT stands for room temperature. The boundary condition at the fire side is simply given as the measured front face temperature $T_f^{exp}(t)$, *i.e.*

$$T(0, t) = T_f^{exp}(t). \quad (9)$$

There are two possible boundary conditions at the back side of the panel, *i.e.* an insulated back face, where upon

$$\frac{\partial T(x = h, t)}{\partial x} = 0, \quad (10)$$

or constant room temperature at the back face, where upon

$$T(x = h, t) = RT. \quad (11)$$

In reality, neither of the ideal boundary conditions represented in (10) and (11) would work well. A simple ‘‘mixture boundary condition’’ is thus proposed as

$$T(h, t) = \alpha T^{eq.(10)}(t) + (1 - \alpha) T^{eq.(11)}(t), \quad (12)$$

where $0 \leq \alpha \leq 1$ is a mixture parameters, and $T^{eq.(10)}(t)$ and $T^{eq.(11)}(t)$ are the solutions obtained using the boundary conditions (10) and (11) at each current finite difference step respectively.

Figure 22a shows the temperature profiles at different positions in one of our composite panels. This panel will hereafter be referred to as Case 1. The theoretical results are in good agreements with the experimental curves. The out-of-plane thermal conductivity k was taken at $0.25 \text{ watt}/(m \cdot ^\circ C)$, ρ as $1.6 \times 10^3 \text{ kg}/m^3$, C_p as $1.5 \times 10^3 \text{ J}/(kg \cdot ^\circ C)$ and $\alpha = 0.5$. Figure 22b shows the through thickness temperature distribution profiles at 5 different first exposure times. These more detailed thermal distributions were obtained by interpolating using the theoretically computed temperature profiles.

7.2 Material Degradation Profile for Case 1 (High-Fiber Density Materials)

The next step, after the thermal analyses, is to determine the property degradation profile *versus* temperature. As noted earlier, an ideal property degradation curve obtained by fitting to a measured reduction if flexural and in-plane stiffness was used (see Figure 1a). It is assumed that all components of the elasticity

tensor, in addition to the interlaminar shear strength, follow this master degradation curve. The figure makes clear that at temperatures below $100^{\circ}C$, the degradation is not significant; at temperatures about $100^{\circ}C$, the modulus drops rapidly and quickly approaches zero at about $130^{\circ}C$.

With the information available in Figures 1 through 15 and 23, through-thickness degradation profiles can be obtained. Figure 23 shows such a plot of through-thickness degradation profiles at several different fire exposure times. It is interesting to note that, at $t = 75min$, 36 percent of the material is completely damaged with zero compressive load bearing capacity. The progression of damage *versus* time is also evident.

7.3 Structural Analysis of Case 1 (High-Fiber Density Materials)

With all the degraded property profiles in hand, a structural analyses can be performed. Using the model presented in Section 6.1 (*cf.* equation (3)) and by taking the values of E_f , E_b and E_c as shown in Figure 23, a critical load *versus* time profile can be calculated as illustrated by the solid line label “3-parameter model” in Figure 24.

With the applied in-plane load of $6.67kN$ ($1500lbs$), the predicted failure time was found to be about $72min$. The actual measured failure time was $65min$ (see the measured out-of-plane displacement *versus* time curve). The out-of-plane displacement goes up very quickly when approaching the failure time. Considering the $1.33kN$ ($300lbs$) out-of-plane load applied in the experiment, which would contribute to failure, the match is fairly good.

7.4 A Two-Parameter Model and Analysis of Case 1 (High-Fiber Density Materials)

To further simplify the modelling approach, *i.e.* by reducing the number of engineering parameters needed as input, a two-parameter is developed as described below.

By examining the degradation profile shown in Figure 23 and looking ahead to Figure 26, it is clear that the load is mostly carried by the unexposed half side of the panel, especially when approaching the failure time. Another observation is that, along the unexposed half side, the temperature distribution is quite close to linear during the whole degradation process (see Figure 22b, and also looking ahead to Figure 25b). This means that, linear interpolation between T_c and T_b can quite accurately describe the temperature distribution profile of the unexposed the half side, and therefore may adequately describe the load bearing capacity of the unexposed half side with the help of the master degradation profile (Figure 1a). Here we define T_f , T_c and T_b as the fire side, center, and back side temperatures, respectively. What we do next is, assuming a linear temperature distribution across the whole panel, to estimate T_f by extrapolating from T_b and T_c , for example

$$T_f = T_c + (T_c - T_b) = 2T_c - T_b \quad (13)$$

This assumption leads to a more severe thermal profile than the actual case in the case studies performed.

Using the newly computed T_f , together with T_c and T_b , the degradation profile of Figure 1a can be used to compute the fire side, center, and back side Young’s moduli E_f , E_c and E_b . Thus from (3) and (4), the critical collapse load for the entire panel can be estimated. The result of the two-parameter is plotted against that of the three-parameter model shown in Figure 24, Both models give practically the same failure time prediction for this case, which is about $72min$. (Again close to the measured time $65min$.) We also note in passing that it is to be expected that the observed failure time for this panel would be somewhat lower than that predicted. One reason for this is that this panel had interior thermocouples that served as defects as mentioned above.

This exercise suggests that, the center temperature T_c and the back side temperature T_b (strongly influ-

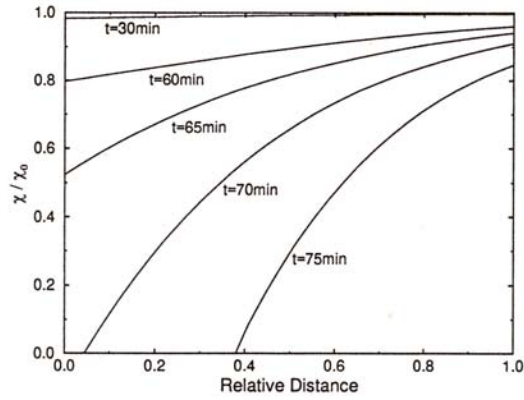


Figure 23: Through-thickness degradation profiles at different times for Case #1.

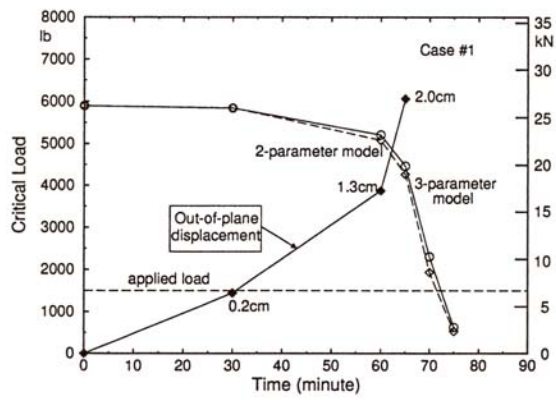


Figure 24: Calculated critical collapse load *versus* fire exposure time along with measured out-of-plane displacement *versus* time for Case #1.

enced by the thermal boundary conditions at the back side) are two of the most influential parameters in structural failure analyses.

7.5 Case 2 (High-Fiber Density Materials)

The results of another panel are described next for which both the thermal and mechanical loadings were less severe than for the panel just reviewed. For this panel the in-plane load was $4.45kN$ ($1000lbs$) and the out-of-plane was $2.22kN$ ($500lbs$). Thermal insulation was used as described earlier but the same E-119 thermal load resulted in a less severe temperature rise as show in Figures 25a and 25b, where the theoretical curves were obtained with $\alpha = 0.1$ in equation (12). The resulting degradation in properties are shown in Figure 26. In this case, the degradation gradients are not linear but can be adequately fit with a curve of the form given by (1). The procedure described in Sections 7.1-7.4 was then applied. The computed results of critical collapse load *verses* fire exposure time for both the three-parameter and two-parameter models are shown in Figure 27, where the estimated failure times are approximately 95 and 90 *min*, respectively. The experimental observed time to failure was approximately $92min$, as evident *via* the out-of-plane displacement *verses* time curve in the figure. The out-of-plane displacement increases rapidly when approaching the failure time and the load bearing capacity drops below the applied load beyond the failure time. Again, good agreement between theory and experiment are found in Case 2 here regarding the time to failure. Note that this panel did not contain interior thermocouples and thus the observed and predicted failure times more closely matched.

7.6 Case 3 and 4 (Low-Fiber Density Materials)

Similar tests were carried out on single skin panels of low-fiber density; these materials were described in Section 2.1. The panel of Case 3, herein, was subjected to $13.3kN$ ($3000lbs$) in-plane load and a $0.89kN$ ($200lbs$) out-of-plane load. Very similar temperature distributions resulted during the combined thermal/mechanical loading.

Figure 28 shows the computed and measured responses. In particular, the figure shows the measured out-of-plane displacement *cross plotted* against the calculated collapsed load, both *verses* the fire exposure time. As before, the predicted failure time is, as indicated in the figure, that time at which the computed collapsed load falls below the applied load. As noted in the figure, this occurs at approximately 28 minutes. The observed failure time was 27 minutes as can be seen by the rapidly rising displacement *verses* time curve.

The good agreement between the calculated and measured failure times demonstrate that the modelling procedures developed for high-fiber density materials work for the low-fiber density materials as well. Results similar to these are shown for a second low-fiber density single skin pane, Case 4, in Figure 29. In this case the applied in-plane load was $18.8kN$ with the out-of-plane load being, again, $0.89kN$. The measured and computed results are again consistent demonstrating the viability of the approach. We note that in this case the failure time was approximately 29 minutes. This slightly larger failure time, given the larger in-plane load was due to the fact that the observed temperature increases in this panel were not quite as severe as in the panel described in Case 3.

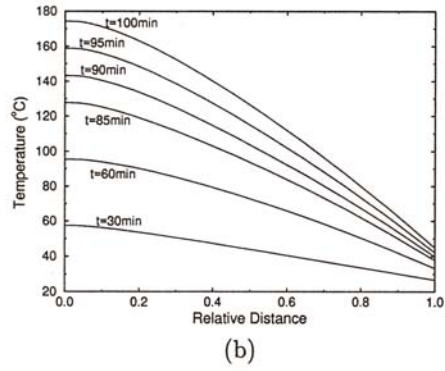
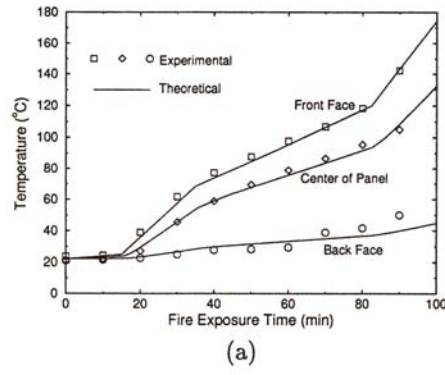


Figure 25: Thermal analysis results for Case #2: (a) temperature *versus* time plots at different panel positions, and (b) temperature distribution profiles at different fire exposure times.

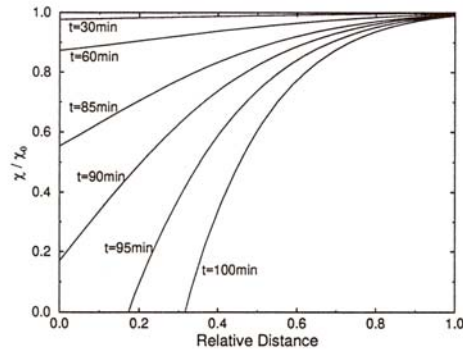


Figure 26: Through-thickness degradation profiles at different times for Case #2.

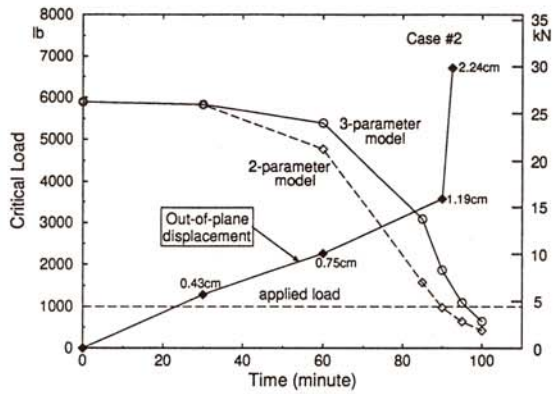


Figure 27: Calculated critical collapse load *versus* fire exposure time along with measured out-of-plane displacement *versus* time for Case #2.

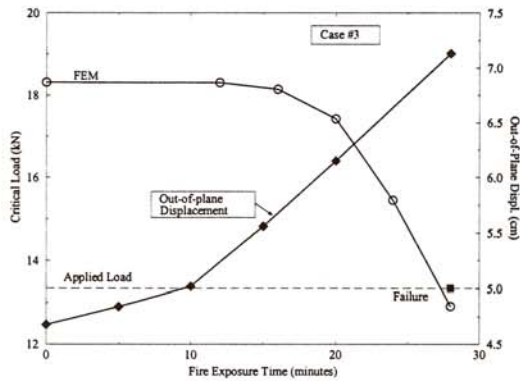


Figure 28: Calculated critical collapse load *versus* fire exposure time along with measured out-of-plane displacement *versus* time for Case #3.

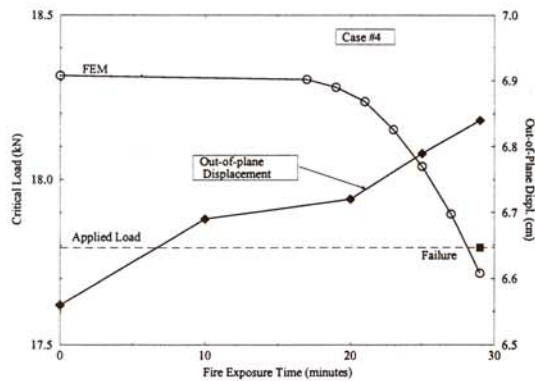


Figure 29: Calculated critical collapse load *versus* fire exposure time along with measured out-of-plane displacement *versus* time for Case #4.

8 Discussion on Design Criteria for Single Skin Panels

8.1 General Discussion

With the case studies presented in Section 7, we now seek possible design criteria. Similar to the case for aluminum alloys, a collapse load *verses* center temperature criterion is evaluated.

As discussed earlier in Section 7.4, the center temperature T_c and the back side thermal boundary condition (*i.e.* T_b) are two of the most influential factors in structural failure analyses. Now we are seeking to understand the relationship of the critical collapse load P_{coll} to these two factors. We develop the approach using Case 1 and Case 2 as examples.

For Case 1 represented in Figures 22 through 24, we first fix the temperature-time history at the front face of the panel, and choose two extreme back face thermal boundary conditions, *viz*: 1) an insulated back face, and 2) a constant back face temperature $T_b \equiv RT$ (again RT is room temperature). The procedure described in Sections 7.1 - 7.3 is then applied to computer the critical collapse of load P_{coll} , and the results are plotted against the center temperature T_c as shown in Figure 30. The master degradation curve labels χ/χ_0 , is also shown in the figure for reference. As indicated in the figure, the insulated back face curve closely approximates the master degradation curve. The experimental curve is seen to fall between the two extreme cases but more closely to the insulated back face curve.

A similar analysis can be performed for the second panel and the results are shown in Figures 25 to 27. In Figure 31, the experimental curve is plotted against the results using two extreme back face thermal boundary conditions; the master degradation curve is also shown in the figure. Again, we observe that the insulated back face curve lies close to the master degradation curve, while the experimental curve is seen between the two extreme cases but closer to the $T_b \equiv RT$ curve.

From Figures 30 and 31, the areas between the two extreme back face thermal conditions can be described as a “danger zone” for both Cases 1 and 2. A panel subject to a load above the “danger zone” will not survive the fire danger; a load below the “danger zone” will be safe; and the safety of any load is between will depend on the actual thermal boundary conditions. Another interesting observation is that, although the two cases have quite different thermal/mechanical history *versus* time, they have similar “danger zones”.

The “danger zone” approach is conceptually similar to the design criterion used with aluminum alloys as described and discussed in Section 1. The difference is that, for aluminum alloys, the “danger zone” collapses to a single line - the collapse load *verses* temperature curve, and a uniform temperature across the panel thickness can be assumed.

A further step can be taken which focuses on a *critical penetrant heat flux (CPHF)* that, given assumed boundary conditions on the exposed face, would lead to a critical temperature at the panel’s center. For example, the boundary value problem described in the inserts of figure yields that results shown in Figures 32a and 32b; *i.e.* a set of curves of incident heat flux *versus* time to reach a given temperature at the panels center. Note that the curves shown in Figures 32a and 32b were computed for a single skin panel of the constituent material of the Case 1 and Case 2 panels described earlier; the thickness taken here was $12.5mm$. Scaling with panel thickness is straightforward: if x_{1c} and t_1 are the half thickness and time it takes to reach a given temperature at the panel’s center for one panel, and x_{2c} the half thickness of a second panel, the corresponding t_2 is $t_2 \approx t_1 \sqrt{x_{2c}/x_{1c}}$.

Next return to Figures 30 or 31 and assume the $P_{coll}/P_{coll}^0 \leq 0.5$ represents a structurally unsafe condition because an original factor of safety of two (2) was used in design. The procedure for extracting a critical panel center temperature is the same as discussed earlier in Section 1.3 and in connection with Figure 17. For this purpose we use the approximate mid range of the “danger zones” ; this yields a critical temperature of $T_{crit} \approx 115^{\circ}C$. According to Figure 32b, which assumes the back face to be constant at room temperature ($RT = 20^{\circ}C$), correlations between the incident heat flux and the time it takes to achieve T_{crit} at the panel’s

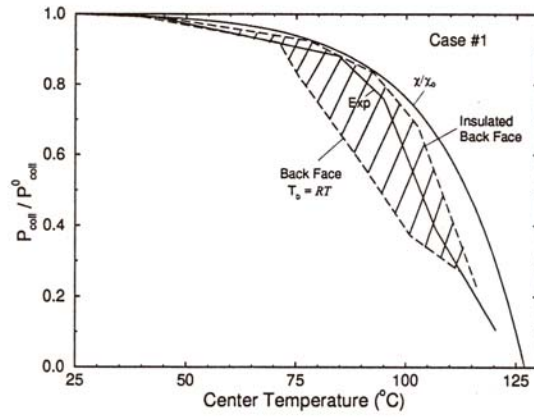


Figure 30: Critical collapse load *versus* center temperature T_c for Case #1.

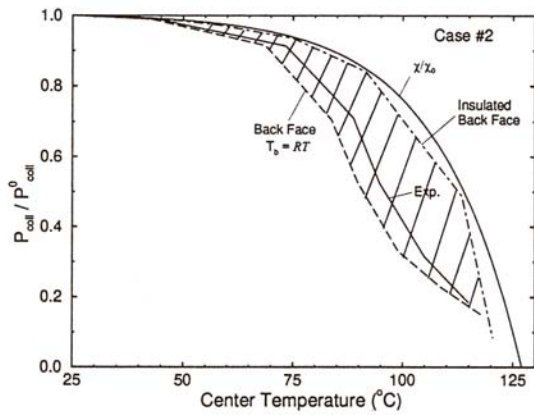


Figure 31: Critical collapse load *versus* center temperature T_c for Case #2.

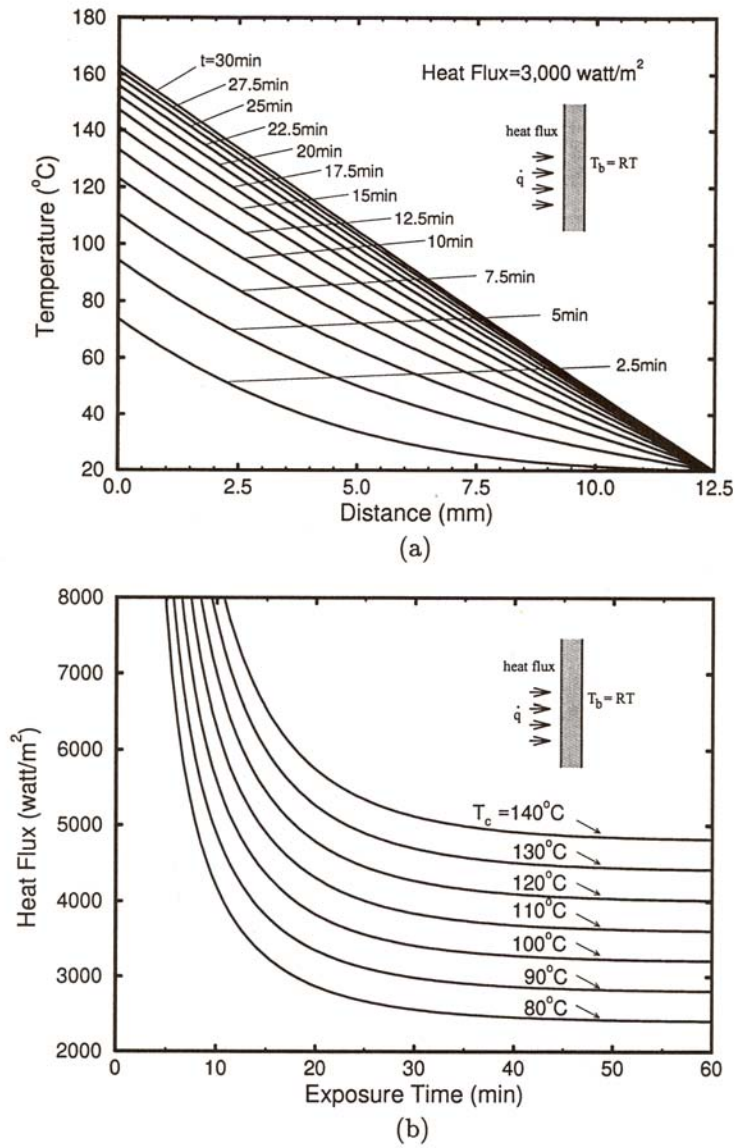


Figure 32: (a) Temperature distribution profiles at different fire exposure times with $\dot{q} = 3,000 \text{ watt/m}^2$, obtained by solving the thermal boundary value problem described in the insert; and (b) incident heat flux \dot{q} needed *versus* the times it takes to achieve different panel center temperatures.

center can be directly obtained. Once a *fire protection time* is prescribed the CPHF can be determined. This provides a clear performance requirement for thermal protection by coatings, insulation, or other fire mitigating systems.

For panels fabricated from a low-fiber density materials a similar approach is possible, but this leads to the identification of critical temperature that are somewhat lower. For example, the ratio of applied load to the undamaged collapsed load in Case 3, is approximately 0.72. The temperature at the panel’s center at collapse was approximately $80^{\circ}C$. To contrast this with the behavior of high-fiber density materials, we examine Figures 28 and 29. For these materials P_{coll}/P_{coll}^0 falls to levels on the order of 0.72 only after temperatures near $100^{\circ}C$ are reached in the center of the panel. In other words, the temperatures at which the comparable losses in load bearing capacity occur in low-fiber density materials, *verses* high-fiber density materials are, in turn, about 0.8 of those for high-fiber density materials. For high-fiber density materials, P_{coll}/P_{coll}^0 falls to 0.5 at the panel center temperature of approximately $115^{\circ}C$; for low-fiber density materials P_{coll}/P_{coll}^0 is expected to fall to levels of 0.5 at panel temperatures of approximately $90^{\circ}C$. This again suggests that the temperatures at which panels of low-fiber density materials lose comparable structural integrity, as do panel of high-fiber density materials, are some 75 to 80 percent of the temperatures for high-fiber density materials.

Descriptions of failure in cored panels will, for reasons discussed earlier in Section 1.4, be more complex. For example, skin wrinkling is one such important failure mode to be carefully studied along with structural buckling. Experimental studies are currently underway of structural collapse in cored, *i.e.* sandwich, panels subject to combined thermal and mechanical loads. These are being complimented by detailed computational simulations; the failure mechanisms and criteria listed in Figure 18 serve as guides. A few examples of sandwich panel failure are described next.

8.2 Single Skin Design and Test Methodology

We begin by examining Figures 30 and 31 along with specifying a structural design factor of safety; for illustration we take the factor of safety to be 2. Accordingly, when P_{coll}/P_{coll}^0 falls below 0.5, the structure is unsafe at elevated temperatures, *i.e.* during the fire. This occurs when the panel’s center temperature, T_c , reaches about $115^{\circ}C$ for high-fiber density materials and $90^{\circ}C$ for low-fiber density materials. Alternatively the material properties at the panel’s center, represented by χ in Figures 30 and 31, have been reduced to approximately 0.75 of the original values. Thus to insure that such a single skin panel does not lose more than one-half of its original compressive load bearing capacity it is necessary that the center temperature not exceed $115^{\circ}C$ or not lose more than 25 percent of its original stiffness.

8.3 A Simple Single Skin Test with Validation

A simple thermal screening test could be utilized to qualify single skin materials *vis-a-vis* structural integrity. The required panels could have minimum in-plane dimensions of $500mm \times 500mm$ and be no thicker than $10mm$. Such panels would be subject to a temperature *versus* time history corresponding to the prescribed by IMO Resolution A. 784 (18) for times up to $60min$. It is noted that this history is similar to that prescribed in the E-119 standard. Boundary conditions would be as illustrated in Figure 33. The panel edges should be insulated whereas the back, unexposed, face would be held at ambient temperature, *e.g.* $20^{\circ}C$. Thermal protection would be applied to the exposed face where it is anticipated that such protection would be either a coating, co-molded intumescent layer(s), *etc.*

The panel’s center temperature *versus* time would be recorded over the $60min$ test duration. With a specified structural factor of safety, which translates to a maximum panel center temperature *via* Figures 30 and 31, it is necessary that the measured panel center temperature not exceed this maximum temperature for the specified fire protection time. A procedure for this would be to plot the measured T_c *versus* time as illustrated in Figure 34. The specified, or desired fire protection time must be less than t_{max} as illustrated in the figure.

The validation of the test could proceed as follows. Having determined a time when the panel’s center

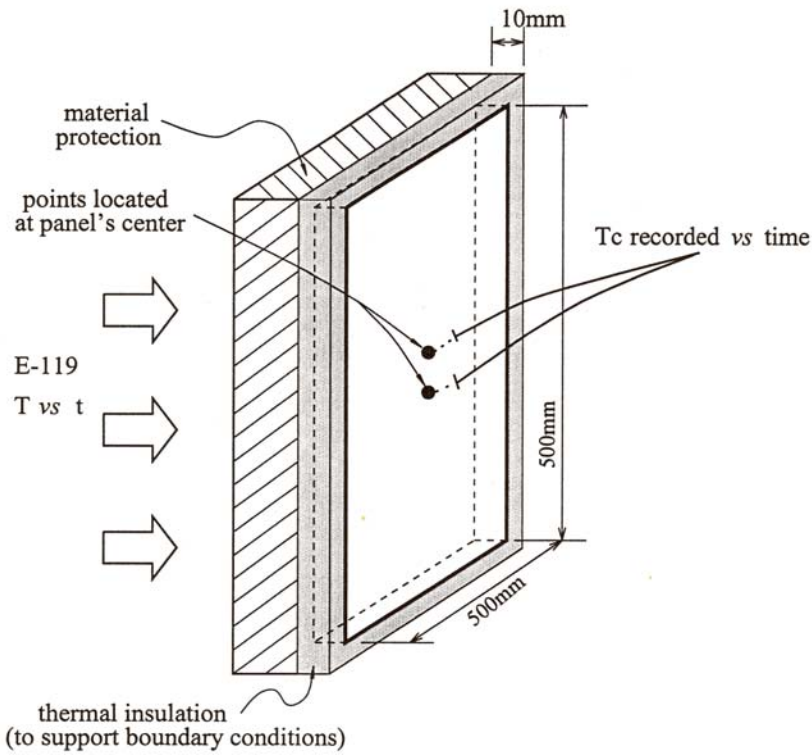


Figure 33: Schematic drawing of a proposed simple thermal screening test setup for single skin panels.

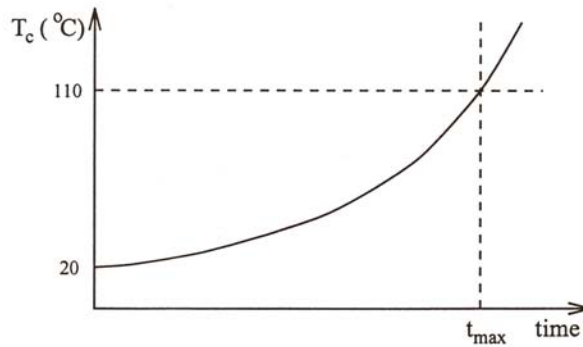


Figure 34: When $T_c \leq 110^\circ\text{C}$ is specified for a single skin panel, the measured T_c versus time curve can be plotted. The specified, or desired fire protection time must be less than t_{max} as illustrated in the figure. The ambient temperature is 20°C .

temperature reached T_c for a given load, *e.g.* one-half the design load, a structural panel test is to be performed where that load is applied, in-plane. The out-of-plane load is to be 5 percent of the in-plane load. It is expected that the collapse time would be within, say ± 10 percent of t_{max} . Such confirmation would provide validation of the procedure.

9 Failure Modes in Sandwich Panels

9.1 Perspective on Sandwich Panel Failures

Figure 18 illustrated three common failure modes that occur in sandwich panels subjected to compressive loads. Of these two appear to be particularly important *vis-a-vis* thermally damaged materials; they are 1) skin wrinkling which may, in turn, lead to delamination, and 2) structural buckling. Both modes are more highly dependent on core properties than on skin properties. For example, in the case of structural buckling, if the core properties were to be so severely damaged so that $P_C \equiv (bd^2/c)G_C$ nearly vanished, the overall buckling load would appear $P_{coll} \rightarrow P_C$, *i.e.* independent of skin properties. In the definition of, P_C , G_C is the core's shear modulus, c the core thickness, and b is the overall sandwich panel thickness. The third thickness dimension, d , is distance from the centers of the panel's face skin. There is, of course, a tacit assumption in this that the panel is rather slender.

In general, the critical load for structural buckling, as depicted in Figure 18, can be expressed as [12]

$$P_{crit} = P_E \left\{ \frac{1 + P_{Ef}/P_C + (P_{Ef}/P_C)(P_{Ef}/P_E)}{1 + P_E/P_C - P_{Ef}/P_C} \right\} \quad (14)$$

where

$$P_E = \frac{\pi^2 EI}{L^2} \quad P_{Ef} = \frac{\pi^2 EI_f}{L^2} \quad P_C = \frac{bd^2}{c} G_C$$

where P_E represents the Euler buckling load of the sandwich panel as estimated by neglecting core shear strains, P_{Ef} represents the sum of the Euler loads of the two faces when they buckle as independent panels, (*i.e.* when core is absent), and P_C may be described as the shear buckling load. In the above, $E = E_f/(1-\nu_f^2)$ is the equivalent Young's modulus of the panel faces and, again, G_C is the shear modulus of the core.

On the other hand, assuming thick sandwich construction, (*i.e.* when the core thickness c is much greater than the face thickness f), the critical conditions of skin wrinkling can be expressed as [13].

$$P_{crit} \approx 3bf \left\{ \frac{1}{6(1-\nu_f^2)} E_f G_C E_C \right\}^{1/2} \quad (15)$$

where E_C is the transverse Young's modulus of the core.

Figure 35 illustrates a particular example of a cored panel with a relatively thin skin thickness $f \approx 1.5mm$ ($0.66in$) and core thickness of $c \approx 25.4 - 50.8mm$ ($1 - 2in$). Typical composite properties for the sandwich panel (E-glass/vinylester skin and PVC core) are given as $E_C = 66.2MPa$ ($9600psi$), $G_C = 25.5MPa$ ($3700psi$), $E_f = 20.7GPa$ ($3msi$), and $L = 0.38m$ ($15in$). The figure illustrates the critical loads *versus* core thickness consistent with the above range. Note that the tendency is for panels with thicker cores to undergo wrinkling type failures whereas the thinner cores buckling loads are lower, leading to the expectation of buckling failures. Core, or skin, degradation can not only lead to a decrease in the critical loads but can also lead to change in the failure mode. To do further, it is necessary to verify that above analytical formulae which is done next.

However, when dimensions are taken to be comparable to typical panels used in HSC craft construction, *viz.* skin thickness of $f \approx 5.1 - 10.2mm$ ($0.2 - 0.4in$) and core thickness of $c \approx 25.4 - 50.8mm$ ($1 - 2in$) and the slenderness ratio $L/(2f + c) \approx 30 - 50$, the critical loads computed from equations (14) and (15) respectively have the relation

$$3.53 \leq \frac{P_{crit}(wrinkling)}{P_{crit}(buckling)} \leq 9.36. \quad (16)$$

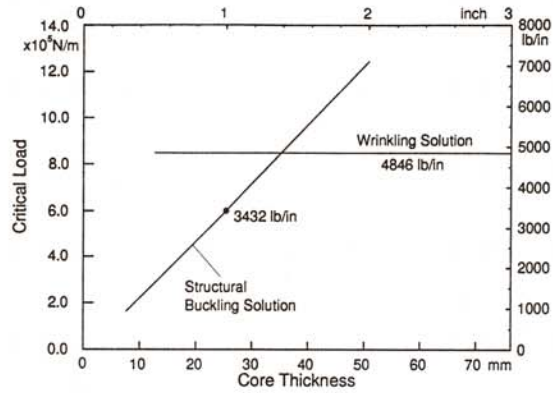
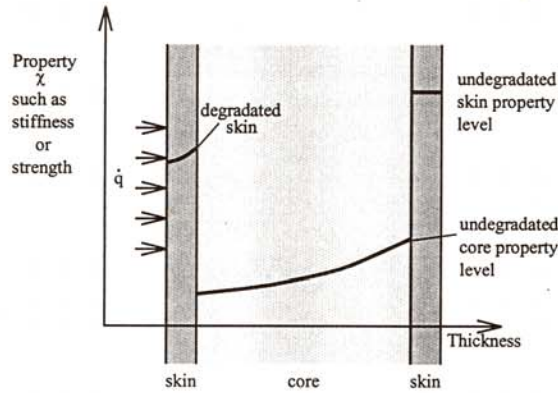
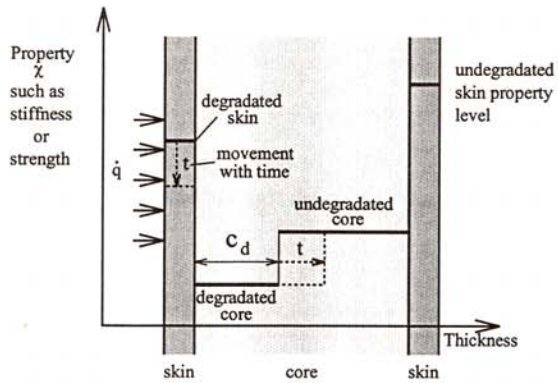


Figure 35: Critical load *versus* core thickness. The panel skin thicknesses are taken as $f \approx 1.5\text{mm}(0.06\text{in})$ and the length as $L = 0.38\text{m}(15\text{in})$.



(a) Sandwich panel property degradation



(b) A simplified damage model for sandwich panels

Figure 36: Schematic drawings of (a) sandwich panel property degradation, and (b) a simplified damage model for sandwich panels.

Table 2: Critical Wrinkling Load *Versus* Imperfection and Core Thickness. For all cases shown in this table the skin thickness was taken as $f \approx 1.5\text{mm}$ (0.6in)

c	$\lambda_c r$	P_{cr}
50.8 mm (2 in)	20 mm (0.8 in)	8.5×10^5 N/m (4866 lb/in)
50.8 mm (2 in)	20 mm (0.8 in)	8.1×10^5 (4622 (lb/in)
63.5 (2.5 in)	20 mm (0.8 in)	8.6×10^5 N/m (4900 lb/in)
25.4 mm (1 in)		8.5×10^5 N/m (4862)
25.4 mm (1 in)		5.9×10^5 N/m (3376)
—	21.6 mm (0.85 in)	8.5×10^5 N/m (4846 lb/in)
25.1	—	6.0×10^5 N/m (3432 lb/in)

Apparently, therefore, for the slender panels typically found in HSC craft construction, structural buckling is the anticipated failure mode. Of course, and as noted earlier, this assumes that the panel's fabrication is of a high quality and that the defect content is low.

9.2 Finite Element Results

Using the material properties specified in Section 9.1, finite element calculations were carried out with three different core thicknesses, *viz.* $c = 25.4\text{mm}$ (1in), $c = 50.8\text{mm}$ (2in) and $c = 63.5\text{mm}$ (2.5in). From Figure 35, the analytical solution for the lesser of the two critical loads for the three cases are seen to be $6.0 \times 10^5 \text{N/m}$ (3432lbs/in, for buckling), $8.5 \times 10^5 \text{N/m}$ (4846lbs/in, for wrinkling), respectively. Note that as the core thickness increases above 50.8mm (2in) that wrinkling (for this short 381mm (15in) long panel) dominated the failure. Five cases were studied numerically using different types of imperfections; the results are summarized in Table 2. A small imperfection magnitude was given as 2.5 percent of the total panel thickness throughout this study. There were three major failure modes appearing in the finite element results; symmetric wrinkling (local failure more), asymmetric wrinkling (local failure mode), and structural wrinkling (global failure mode). The failure modes are, from top to bottom, symmetric wrinkling, asymmetric wrinkling, symmetric wrinkling, and structural buckling, respectively.

9.2.1 Wrinkling Load versus Imperfection and Core Thickness

For the cases with core thickness $c = 50.8\text{mm}$ (2in) and $c = 63.5\text{mm}$ (2.5in), to induce panel collapse, two types of small initial imperfections were applied: 1) two shallow sinusoidal dents symmetrically placed on both skins in the center panel, and 2) one shallow sinusoidal dent asymmetrically placed on only one skin in the center of the panel. The imperfection magnitudes taken in this study are about 1 percent of the panel thickness, and the imperfection wavelength is given as 503.8mm (2in). Finite element computations were performed using the ABAQUS finite element code. The first three cases shown in Table 2 all demonstrate wrinkling with both imperfection forms, and the critical loads so obtained are in very good agreement with the analytical solutions (see Figure 35 and Table 2). The results show that the wrinkling load is relatively insensitive to the imperfection form and core thickness.

9.2.2 Failure Mode Change with Core Thickness

For the case with a core thickness $c = 25.4\text{mm}$ (1in), again we applied the above two types of initial imperfections (see Table 2). From Figure 35, the theory predicts structural buckling as the failure mode with a critical load of $6.0 \times 10^5 \text{N/m}$ (3432lbs/in). However, if we ideally force the boundary condition to be strictly symmetric (*i.e.* forcing the wrinkling deformation), the result is very close to the predicted wrinkling solution. Otherwise, for the asymmetric imperfection form in the last case, the failure mode is a structural buckling type (macroscopic failure mode) with a critical load very close to the predicted structural buckling load.

The preliminary results just described serve to illustrate that the analytical models for failure *via* structural buckling or wrinkling of cored panels may be adequate for basing a design approach. What is needed, however, is a viable method for including material degradation in this approach. This is dealt with next in two contexts, *viz.* one for short panels where both wrinkling and buckling may compete as failure modes and one for slender panels where structural buckling is the prevalent failure mode as discussed in Section 9.1.

~~9.2.3 Failure Mode Change with Core Thickness~~



~~For the case with a core thickness $\epsilon = 25.4\text{mm}$ (1in), again we applied the above two types of initial imperfections (see Table 2). From Figure 35, the theory predicts structural buckling as the failure mode with a critical load of $6.0 \times 10^5 \text{N/m}$ (3432lbs/in). However, if we (ideally) force the boundary condition to be strictly symmetric (*i.e.* forcing the wrinkling deformation), the result is very close to the predicted wrinkling solution. Otherwise, for the asymmetric imperfection form in the last case, the failure mode is a structural buckling type (macroscopic failure mode) with a critical load very close to the predicted structural buckling load.~~

10 Simplified Damage Models for Sandwich Panels

10.1 A Simplified Damage Model for Short Sandwich Panels

To study the fire degradation of sandwich panels, a simple model approach is schematically described in Figure 36. Figure 36a schematically illustrates a property degradation profile across the sandwich panel that may result in during an actual thermo-mechanical test; the back-side skin is assumed to be unaffected. Figure 36b show a simplified damage model. The fire-side skin is assumed to have a representative uniform property which degrades with fire exposure time, t . The degradation in the core is described by an increasing degradation thickness $c_d(t)$, where a representative degradation core property is assumed over the length of c_d . The rest of the panel, including part of the core and the back-side skin, is assumed to have undergone no damage at time t .

Suppose, as an example, the fire exposed skin has the damaged properties $\chi_f = \chi_f^0/3$, and the damaged core thickness $c_d = 0.4c$ with effective properties $\chi_c = \chi_c^0/2$. Using the undergraded properties as used in Section 9.2 with the core thickness $c = 50.8mm$ ($2in$), a finite element calculation was performed with the damaged configuration; the initial imperfection is given as symmetrically placed. Figures 37a and 37b show the undeformed and deformed mesh of the partially damaged sandwich panel, respectively. Although the initial geometric imperfection is symmetric, due to the asymmetric material property degradation, the deformation is not symmetric at all. The critical load calculated for this case is $P_{crit} = 6.3 \times 10^5 N/m$ ($3610lbs/in$). The failure mode is wrinkling. Compare with the undamaged critical wrinkling load $P_{crit} = 8.5 \times 10^5 N/m$ ($4846lbs/in$), there is a more than 25 percent degradation in terms of critical load bearing capacity.

As time progresses the exposed skin and core properties degrade further and, in particular, the extent of damage in the core, *i.e.* c_d , increases. To gain perspective on this, a series of calculations were carried out in which both c_d and E_{core} (fire damaged part) were varied; the results for the critical loads are shown in Figure 38.

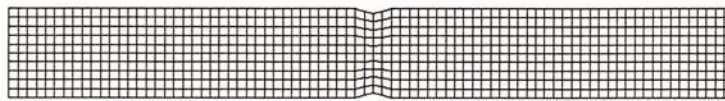
One interesting feature of these results is that after the core is damaged to an extent greater than about 10 percent of its initial thickness the further reduction in the critical load is rather modest until such a point as the core is more than, say, 80 percent damaged. This suggests that the more critical variable is the degree of core damage. In other words, for practical purposes, as long as the core is not “completely” damaged throughout its thickness the precise spatial extent of its damage is of minor importance as compared to degree of damage suffered by its degraded portion. To the extent this is generally true a viable design approach may be based on linking the degradation of the exposed face skin to its adjacent core to the thermal loads. More analyses are required to explore this possibility.

10.2 A Simplified Damage Model for Slender Sandwich Panels

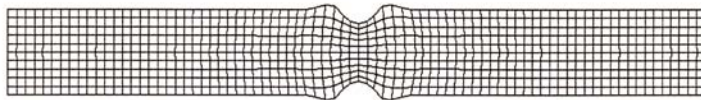
10.2.1 Experimental Results for Slender Sandwich Panels (High-Fiber Density Materials)

Experiments were performed on sandwich panels using similar procedures as described in Section 5. In this series, the panels had identical dimensions but had either a $12.7mm$ ($0.5in$) thick $9lbs/ft^3$ balsa core or an *airlite* foam core. The face-skins were symmetric, $0.356mm$ ($0.14in$) thick, and composed of 2 layers of a 5608-08 quadraxial E-glass/vinylester architecture. During the tests, temperatures were measured on the exposed face (T_f), just behind the exposed face (T_b) *i.e.* at the exposed face/core interface, at the center of the core (T_{mid}), and at the unexposed face (T_0); the temperature at the unexposed face/core interface (T_b) is assumed to be the same as the temperature at the unexposed face T_0 . This assumption was based on the observation that the temperature gradient within the unexposed face-skin were typically shallow. This positioning of thermal couples is illustrated in Figure 39a. The results for two panels fabricated from high-fiber density materials, *via* SCRIMP method, will be described and referred to as Cases 5, 6, and 7 following Cases 1 through 4 described in Section 7 for single skin panels.

Figures 40a, 40b and 40c show the measured temperature profiles as functions of time. It will be noted later that after a relatively short time the average thermal gradients in the exposed skins become nearly



(a)



(b)

Figure 37: (a) Undeformed, and (b) deformed mesh of the partially damaged sandwich panel.

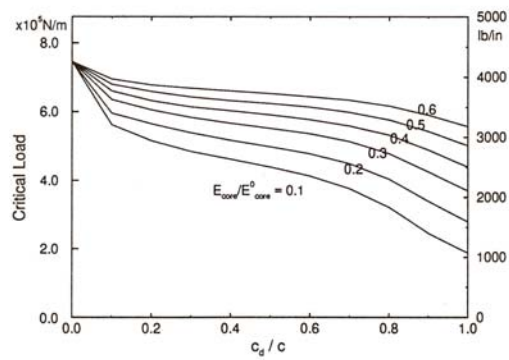


Figure 38: Critical load *versus* the extent of damage c_d and the damaged modulus E_{core} . E_{core}^0 is the undamaged core modulus.

Assume Linear Temp. Distribution

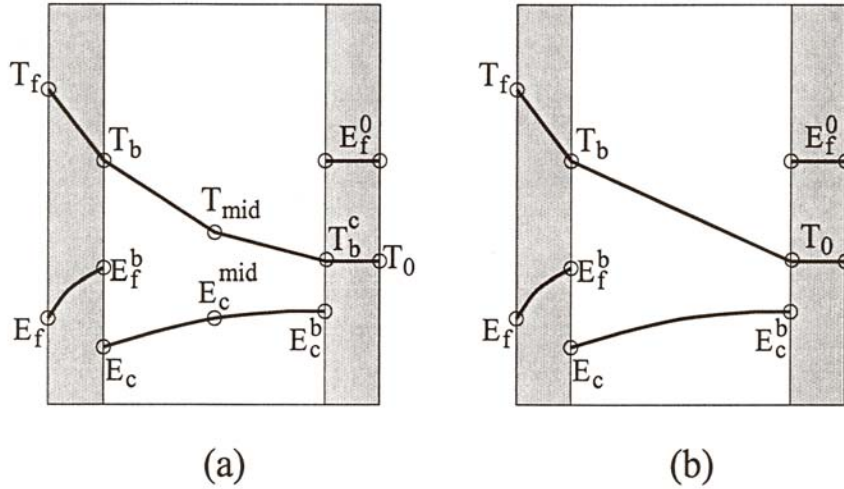
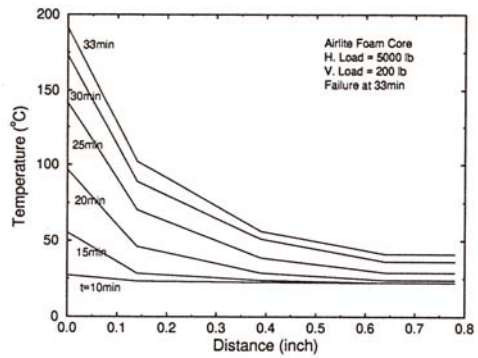
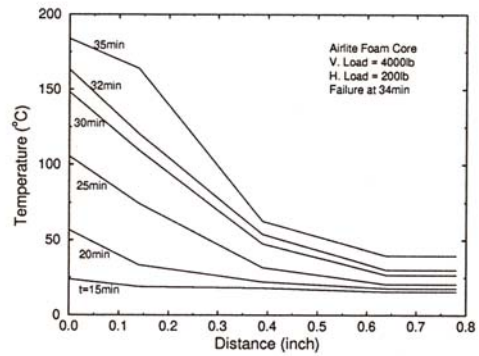


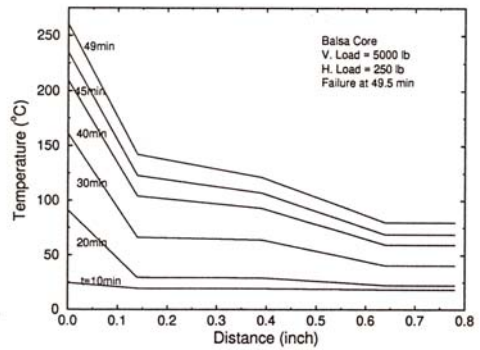
Figure 39: (a) Thermal couple positioning, and the corresponding gradients developed in the sandwich panel. (b) Simplified linear temperature distribution model, where temperature T_b at the exposed face/core interface becomes the most important parameter.



(a)



(b)



(c)

Figure 40: Measured temperature profiles as functions of time within the composite sandwich panels for (a) Case #5 airlite foam core, (b) Case #6 airlite foam core and (c) Case #7 balsa core, respectively.

constant. The temperature rises in the unexposed skin are generally rather modest, at least for time under thirty minutes. At least one-half of the core, however, experiences significant temperature rises and thus degradation in properties. For the airlite form cored panel No. 5, the in-plane load was $22.2kN$ ($5,000lbs$) and the out-of-plane load was $0.89kN$ ($200lbs$); for the airlite foam cored panel No. 6 the in-plane load was $17.8kN$ ($4,000lbs$) and the out-of-plane load was again $0.89kN$ ($200lbs$); for the balsa cored panel No. 7 the in-plane load was $22.2kN$ ($5,000lbs$) but the out-of-plane load was $1.11kN$ ($250lbs$).

Figure 41a, 44b and 41c show the measured vertical displacement *versus* time curves along with the calculated maximum sustainable load *versus* time. The theoretical curves were obtained by using the temperature profiles shown in Figure 40 along with the degradation curves shown in Figure 1 to calculate collapse loads. A small sinusoidal imperfection, with a magnitude of 1 percent of the panel thickness and a wavelength twice the panel length, built into the FEM model, initiate the failure process; the mixture achievable load was taken as the collapse load. It is evident that the predicted times to failure are quite close to those measured. The superior performance of the balsa cord panel is also evident. We next seen to develop a simpler manner in which to describe the thermal profiles *vis-a-vis* the degradation, and loss in load bearing capacity that results. Before doing this, however, a few additional observations on the panel failures are made.

No evidence of delamination was found in both the foam and balsa cored panels. Although this is encouraging it must be noted that the exposed face of these panels were under tension. It remains to be verified by future experiments if this would be the case if the exposed face were in compression. Both the balsa and foam cored panels were reloaded after they had returned to ambient, *i.e.* room temperature. In all cases the panels were able to sustain the original applied in-plane loads of $22.2kN$ ($5,000lbs$) or $17.8kN$ ($4,000lbs$). This indicated that the residual properties were indeed excellent. It remains for future analysis and experiment to explore this further.

It should be noted that the applied in-plane compressive load in these three panels were, as fractions of their initial values as follows: 1) $P_{applied}/P_{coll}^0 = 0.17$ (for Case 5); 2) $P_{applied}/P_{coll}^0 = 0.142$ (for Case 6); and $P_{applied}/P_{coll}^0 = 0.11$ (for Case 7). It should also be noted that the failure times as predicted appear to agree closely with the measured failure times. Predicted failure times would correspond to the time the P_{crit} would just fall below the applied load.

10.2.2 A Simplified Thermal Profile Model

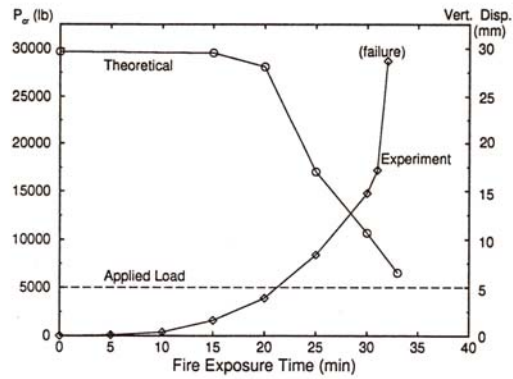
A series of thermal conductivity calculations were performed as depicted in the insert to Figure 42a. Panels were assumed to have skin thickness of between $5.08mm$ ($0.2in$) to $7.62mm$ ($0.3in$) and core thickness of between $12.7mm$ ($0.5in$) to $50.8mm$ ($2in$). On the exposed face skin a constant heat flux was imposed which ranged from $1kW/m^2$ to $5kW/m^2$. The back face was taken to be insulated in these calculations. Figures 42a and 42b show the results of two such calculations for panels having $0.2in$ thick skins. The object of these analyses was to explore the possibility of developing a simple description of the thermal profile through the thickness of a cored panel.

With a constant applied heat flux a relatively constant average thermal gradient is established across the exposed face skin. The two results shown in Figures 42a and 42b indicated that the gradient is roughly proportional to the magnitude of the imposed flux. Additional such calculations have verified this result. Figures 42c and 42d show similar results for the panels with $0.3in$ thick skins and two core thicknesses. These results indicated that the gradient across the exposed face skin is nearly independent of skin and core thickness. Thus to a good approximation the gradient can be taken as $\nabla T \approx 100q^\circ C/(in \cdot kW/m^2)$, or

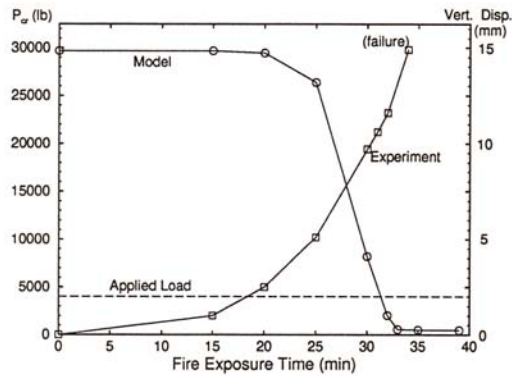
$$\nabla T \approx 3937q^\circ C/(in \cdot kW/m) \quad (17)$$

This allows the construction of an average thermal profile (taken to be linear) across the exposed skin by knowing only a single temperature which we take as the back side of the exposed skin, *i.e.* T_b , as shown in Figure 39a. The temperature, referred to as T_b was described earlier in Section 10.2.1.

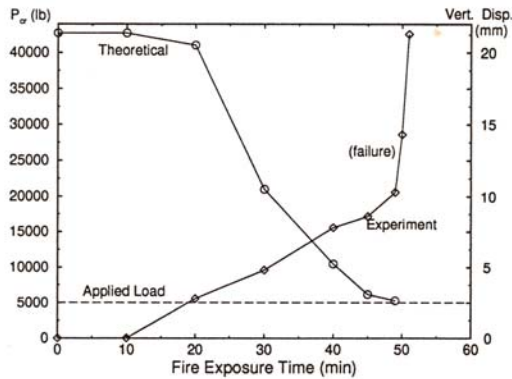
The analyses also indicated that the thermal gradients in the core are also nearly linear. Thus, again



(a)

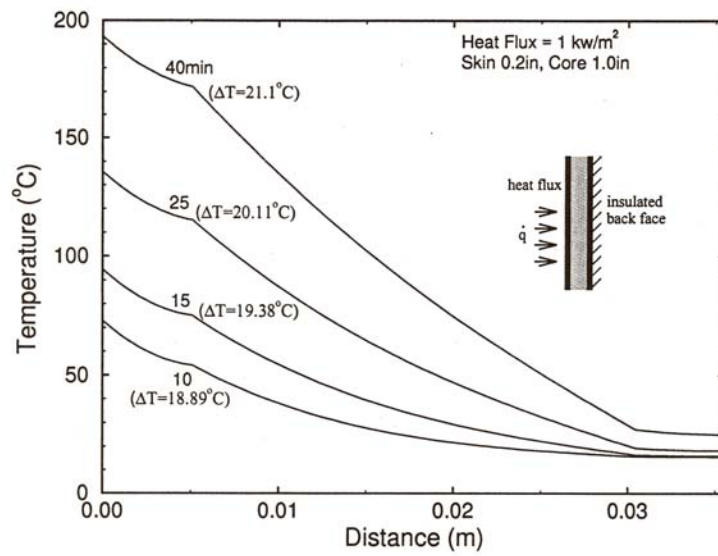


(b)

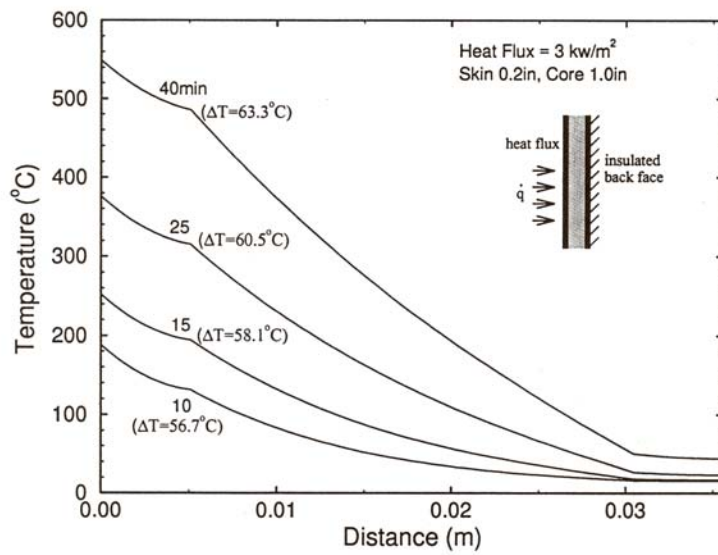


(c)

Figure 41: Measured vertical displacement *versus* time curves along with the calculated maximum sustainable load *versus* time for (a) Case #5 airlite foam core, (b) Case #6 airlite foam core, and (c) Case #7 balsa core, respectively.



(a)



(b)

Figure 42: Thermal conductivity calculations. (a) $\dot{q}=1\text{kw}/\text{m}^2$, with 0.2in skins and a 1in core. (b) $\dot{q}=3\text{kw}/\text{m}^2$, with 0.2in skins and a 1in core.

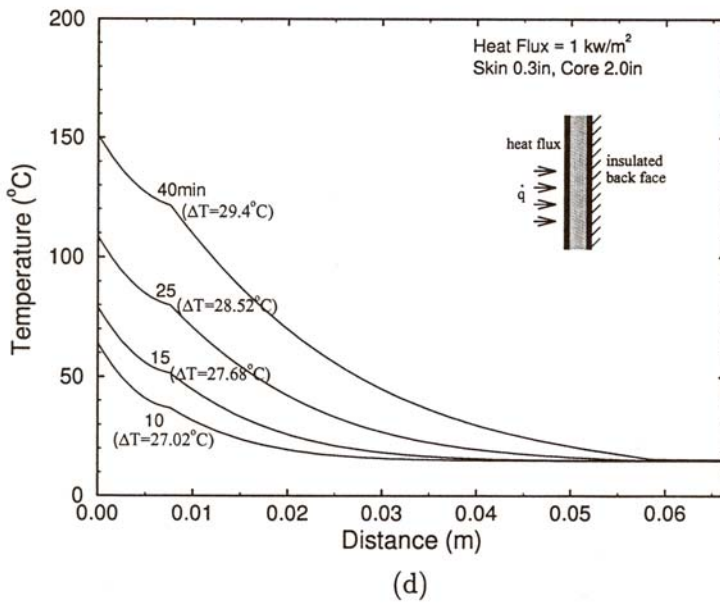
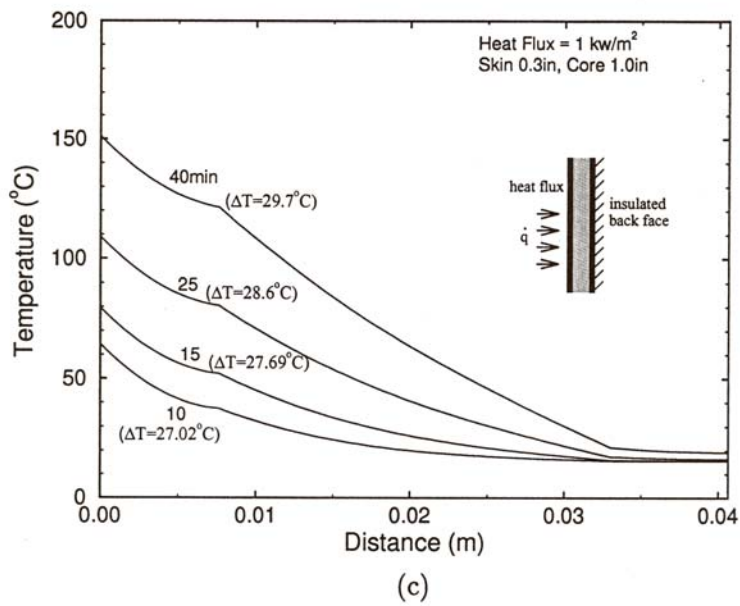


Figure 42 (cont.): Thermal conductivity calculations. (c) $\dot{q}=1\text{kw/m}^2$, with 0.3in skins and a 1in core. (d) $\dot{q}=1\text{kw/m}^2$, with 0.3in skins and a 2in core.

to a good approximation, a linear gradient in the core is established between T_b at the exposed side of T_b at the unexposed side as indicated in Figure 39b. If, furthermore, T_b is taken to be at ambient temperature (or slightly higher) a complete, albeit approximate, thermal gradient is established by the temperature at one point, *viz.* T_b .

A further verification of this approach is obtained by examining the thermal profiles shown in Figures 40a and 40b. We recall that these profiles result from the i,position of a time varying heat flux. However, after a relative short time the thermal gradients appear to become nearly constant. In Figure 40a, for instance, $\nabla T \approx 19685^{\circ}C/m$ ($500^{\circ}C/in$) which would correspond to what would have resulted in a constant, or average, (q) of about $5kW/m^2$ (*c.f.* with relation (17)). *It should be noted that although the heat flux developed in the furnace ranges up to approximately $150kW/m^2$ after 60 min., the heat flux actually penetrating the exposed face-skin is much less. This is explained by recalling that: 1) the panels were insulated with 50.8mm (2in) of mineral wool, and 2) the heat transfer coefficient between the back side of the insulation and the exposed is less than unity. These observations also indicate that heat fluxes in the range of $5kW/m^2$ cause significant damage after times in the range of 20 to 60 min.*

10.2.3 Experimental Results for Slender Sandwich Panels (Low-Fiber Density Materials)

Figure 43 shows the results of two calculations using these types of simplified thermal profiles. Specifically, as shown in Figure 39b, using experimentally measured T_f and T_b and assuming the entire unexposed skin is still at ambient temperature T_o , we can readily construct the simplified linear temperature profiles across the sandwich panel. The measured vertical displacement *versus* time for (a) Case 5 airlite foam core and (b) Case 7 balsa core, respectively. It is clear that the simplified linear model shown with solid lines gives excellent approximations as compared to the original model. The excellent correlation suggests that additional simplifications and assumptions made in the simplified thermal profile model shown in Figure 36b are reasonable.

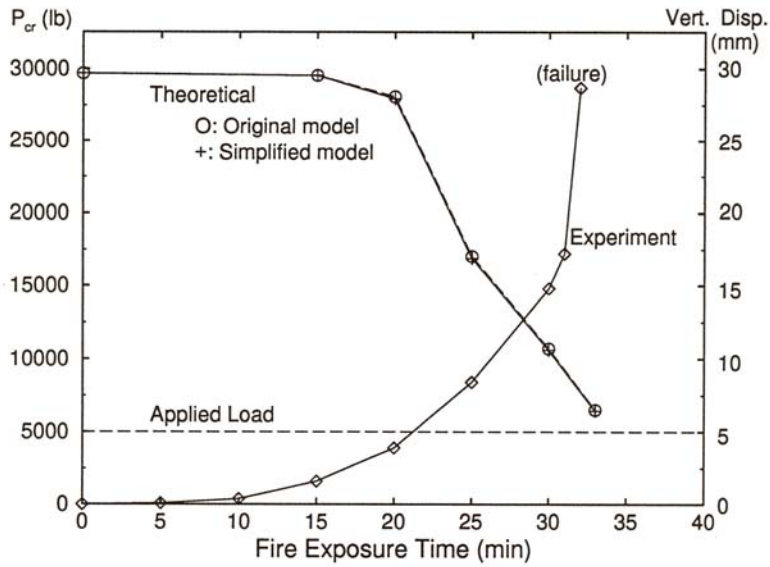
10.3 Experimental Results for Slender Sandwich Panels (Low-Fiber Density Materials)

Similar experiments and analysis were carried out on sandwich panels with face skins fabricated with low-fiber density materials; there will be referred to as Cases 8 and 9. The face-skins in these panels were $3.56mm$ ($0.14in$) thick and has a $12.7mm$ ($0.5in$), $9lbs$ balsa core.

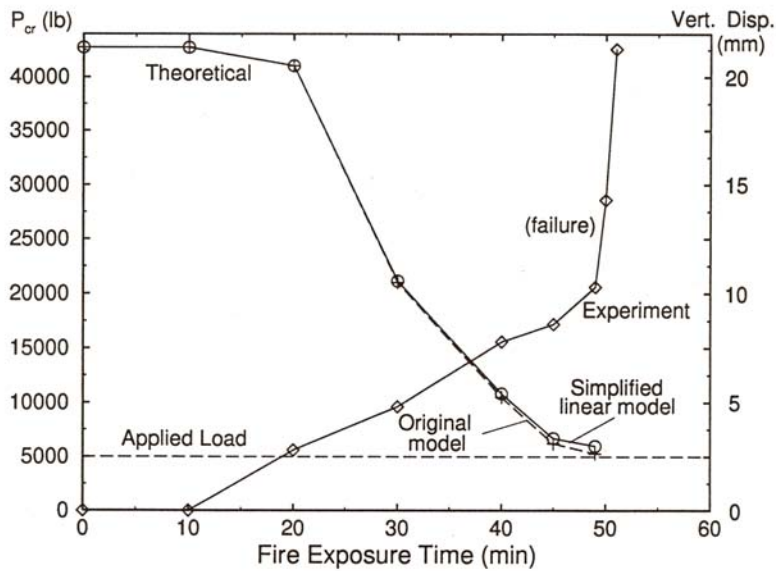
Figure 44 shows the calculated collapse load *versus* fire exposure time along with the measured out-of-plane displacements for Case 8. The in-plane load in this case was $13.34kN$ ($3,000lbs$); the out-of-plane load was again $0.89kN$ ($200lbs$). As before, the measured failure time is indicated by the solid square. Failure was observed, and predicted, to occur at 30 minutes (within 30 ± 2 seconds). The agreement with experiment is thus excellent.

Figure 45 shows similar results for the panel in Case 9. The in-plane load in this case was $17.8kN$ ($4,000lbs$); the out-of-plane load was again $0.89kN$ ($200lbs$). The measured out-of-plane displacement failure at about 29 minutes whereas the predicted failure time is closer to 30 minutes. The agreement between predicted and measured failures nonetheless excellent.

It is worth noting that although the applied in-plane load for the panel of Case 9 was larger than for Case 8, the failure times were similar. It will be explained next, however that this is due to the slower rise in temperature within panel 9. In face, the peak critical temperature within panel 9 were lower than in panel 8. This is as expected due to the higher applied load on panel 9.



(a)



(b)

Figure 43: Measured vertical displacement *versus* time curves along with the calculated maximum sustainable load *versus* time for (a) Case #5 airlite foam core and (b) Case #7 balsa core, respectively. The simplified linear model shown with solid lines gives excellent approximations as compared to the original model.

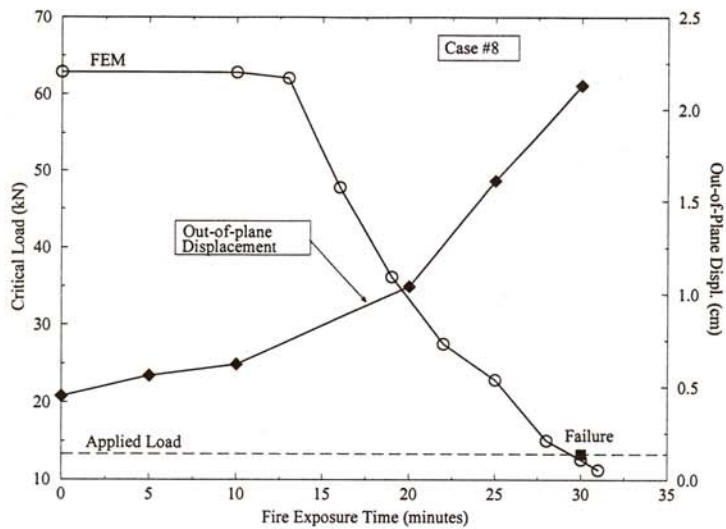


Figure 44: Calculated collapsed load *versus* fire exposure time along with measured out-of-plane displacement for case #8.

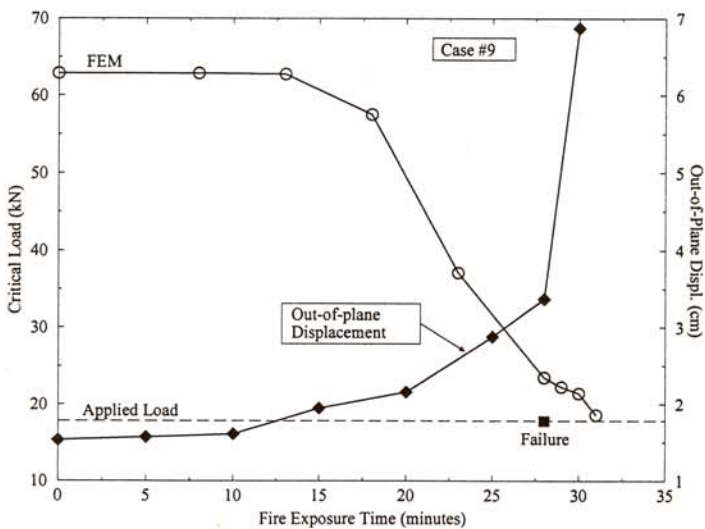


Figure 45: Calculated collapsed load *versus* fire exposure time along with measured out-of-plane displacement for case #9.

11 Sandwich Panel Design and Test Methodology

11.1 Background Discussion

We begin by providing additional perspective on the thermal profile developed in a typical sandwich panel such as illustrated for high-fiber density materials by Case 6 described above. Figure 46 shows both the measured temperatures *versus* time at various locations through the pane thickness and those computed *via* a thermal analysis. The thermal analysis was conducted by applying the E-119 temperature-time history to the exposed face of the 50.8mm (2in) mineral wool layer described in Section 5. For later reference it is noted that the time to failure for this panel was approximately 32 – 34min and that the temperature at the backside of the exposed skin would have been $T_b \approx 120^\circ C$. Again for later reference, it is noted that the applied load of $P_{applied} = 17.8kN$ (4,000lbs) corresponds to $P_{applied}/P_{coll}^0 = 0.142$ (ref. Figure 41b).

Next consider Figure 47 which shows the results of a series of finite element calculations on sandwich panels whose dimensions are listed in the inserted table. This set of calculations were performed using the simplified linear model shown in Figure 39b together with equation (17). Once the temperature at the back side of the exposed skin T_b is chosen in the model, T_f can be obtained from (17); ambient temperature T_0 is taken at $20^\circ C$. Note that for a relatively wide range of panel geometry the curves, when normalized with respect to the undamaged collapse loads, fall within a tight band.

A structural design factor of safety is now assumed and for illustration purposes we will, as in Section 8, take this as 2. This means that if the collapse load, P_{crit} , falls below the panel will lose structural integrity. According to Figure 47 this occurs if T_b exceeds a temperature of approximately $90^\circ C$. Alternatively, if a structural safety factor of 3 were used in the original design, failure would be eminent when $P_{coll}/P_{coll}^0 = 0.33$, or accordingly from Figure 47 when $T_b \geq 115^\circ C$. A practical verification of this approach can be obtained by referencing back to Figure 46 and noting that T_b failure was approximately $120^\circ C$. Figure 47 would indicated, in turn, that the P_{coll}/P_{coll}^0 value associated with $120^\circ C$ is about $P_{coll}/P_{coll}^0 \approx 0.15 \sim 0.17$; the actual experimental value was $P_{coll}/P_{coll}^0 = 0.142$. Similar verifications are found for the other panels that were tested.

Analysis of low-fiber density material panels leads to a prescription of lower critical temperatures. For example, the panel of Case 8, the temperature T_b at failure was measured to be approximately $88^\circ C$; the ratio P_{coll}/P_{coll}^0 at failure was 0.22. Appealing to Figure 44 a high-fiber density panel would be expected to degrade such that $P_{coll}/P_{coll}^0 \rightarrow 0.22$ when T_b rises to valued on the order of $110^\circ C - 115^\circ C$. In addition, Figure 44 indicated that the calculated P_{coll}/P_{coll}^0 would fall below 0.33 when $T_b \approx 65^\circ C$. A quite similar analysis of panel 9 indicates that $T_b \approx 70^\circ C$ when $P_{coll}/P_{coll}^0 \rightarrow 0.22$.

11.2 Sandwich Panel Methodology

We begin by examining Figure 47 along with specifying a typical structural design factor of safety; for illustration take this to be 3.

Accordingly, when P_{coll}/P_{coll}^0 falls below 0.33 the panel is unsafe at at elevated temperatures. This occurs, according to Figure 47 for high-fiber density material panels, when T_b exceeds $115^\circ C$. For low-fiber density material panels this occurs when T_b exceeds $70^\circ C$. *Thus to ensure structural safety, based on an initial structural design factor of safety of 3, the criteria would be that the temperature at the backside of the exposed skin, i.e. T_b , cannot exceed critical value (e.g. either the $115^\circ C$ or $70^\circ C$ value as above) during the specified fire protection time.*

Structural design factors of safety may, of necessity, have to be raised over what would be required for ambient temperature structural design to account for the potential damage caused by fire. Such design considerations will require continued study that indicates considerations of, *inter alia*, cost, overall ship weight, and space.

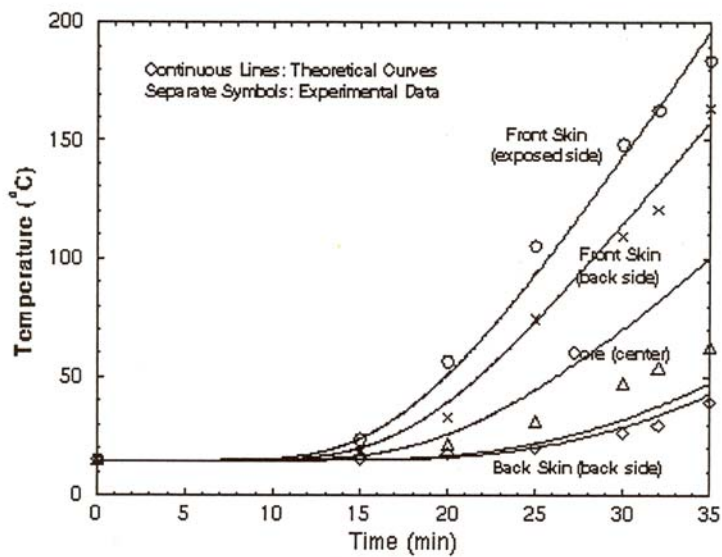


Figure 46: Measured temperatures *versus* time for Case #6 at various locations through the panel thickness and those computed *via* a thermal analysis.

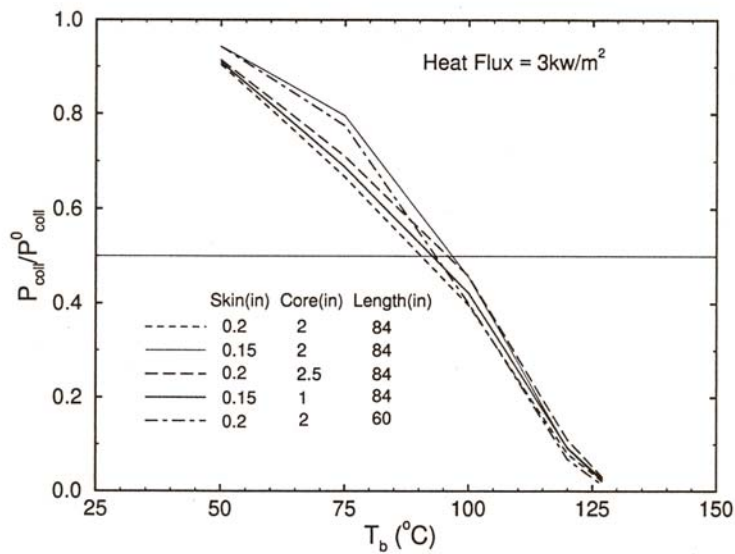


Figure 47: Results of a series of finite element calculations on sandwich panels whose dimensions are listed in the inserted table. This set of calculations were performed using the simplified linear temperature distribution model.

11.2.1 A Simple Sandwich Panel Test with Validation

A simple thermal screening test could be utilized to qualify sandwich panels *vis-a-vis* structural integrity. As for the case of single skin panels, the sandwich panels could have minimum in-plane dimensions of $500mm \times 500mm$ along their specific skin and core architectures. Such panels would be subject to a temperature *versus* time history, as prescribed by IMO Resolution A. 754 (18), for times up to $60min$. Boundary conditions would be as illustrated in Figure 48. The panel's edges should be insulated whereas the back (unexposed) face would be held at ambient temperature, *e.g.* $20^{\circ}C$. Thermal protection would be applied to the exposed face where it is anticipated that such protection would be a coating, sacrificial layer(s), intumescent layer(s), *etc.*

The temperature at the back side of the exposed skin, *i.e.* T_b , would be recorded over the $60min$ test duration. With a specified structural factor of safety, which translates to a maximum T_b *via* Figure 47, it is necessary that the T_b not exceed this maximum value during the also specified fire protection time.

Validation would be achieved by conducting a compressive panel test as described in Section 5. The candidate material protective layer would be applied along with a constant in-plane load corresponding to one-half of the design load. The out-of-plane load would be fixed at 5 percent of the in-plane load. For high-fiber density materials, collapse is expected when T_b reaches a value of $115^{\circ} \pm 10^{\circ}C$. For low-fiber density materials, collapse load is expected when T_b reaches a value of $90^{\circ}, \pm 10^{\circ}$.

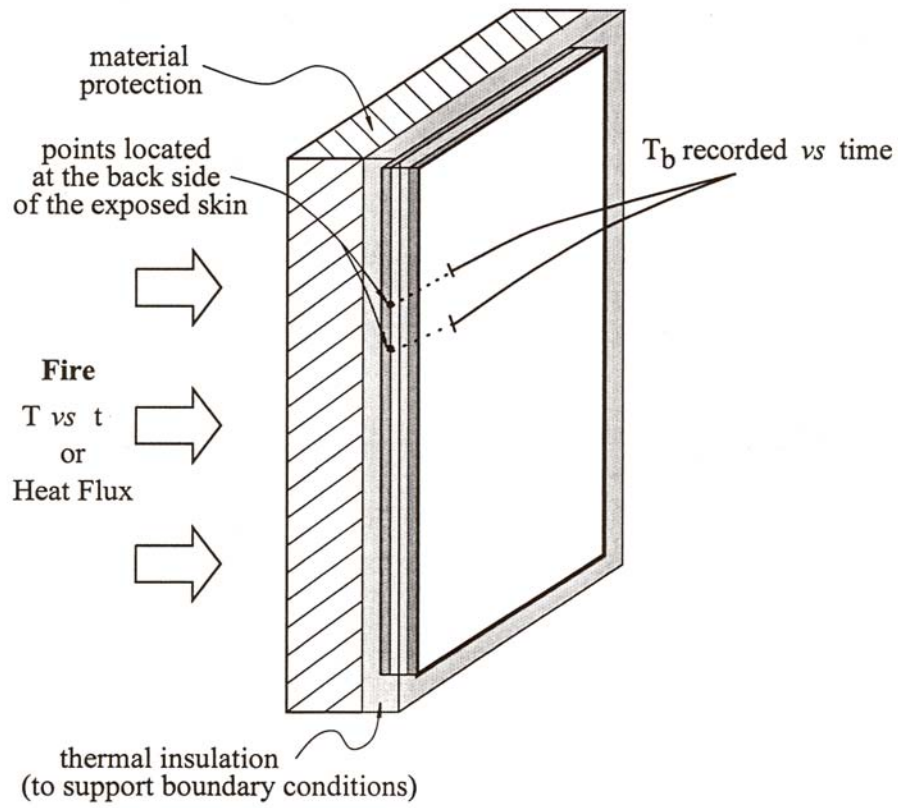


Figure 48: Schematic drawing of a proposed simple thermal screening test setup for sandwich panels.

12 Conclusions

A general framework for analyzing the loss of structural integrity of single skin panels has been outlined and shown to reliably describe the compressive collapse of panels exposed to combined mechanical and thermal loads. The analyses performed have led to the concept of a *critical incident flux* that, when coupled to specifications of structural design safety factors, prescribes the performance requirements of insulating systems. In particular, the specification of a critical incident heat flux prescribes the thermal insulation requirements *vis-a-vis* ensuring adequate load bearing capacity is maintained for the required fire protection times. For cored panels, a model for damaged sandwich panels has been outlined and calculations have indicated an approach to a simple design criterion. This criterion is based on the notion of a damaged exposed skin and its adjacent degraded core. Additional work is needed to refine these concepts. Such future work is described next.

13 Recommendations for Future Work

13.1 Validation *vis-a-vis* Stiffened Panels

The methodology described here was based on testing and analysis of unstiffened panels. The predictive, analysis procedures are quite general, however, and are directly applicable to complex geometries. An immediate next step, accordingly would be to perform both tests, and corresponding analyses, on stiffened panels. The purpose here would be to confirm the accuracy of the methods developed here in describing the structural response, and performance, of panel's 3-dimensional structure. In particular, panels conforming with IMO Resolution A.254 (18), *Recommendation on Fire Resistance Tests for "A", "B", and "C" Class Divisions* and MSC.45(65), *Test Procedures for Fire-Resisting Divisions of High-Speed Craft* should be investigated to confirm that the methods described herein would ensure acceptable behavior *vis-a-vis* those standards.

Stiffened panels should be subject to combined analysis and full-scale testing. Loading should be as prescribed by IMO Resolution A.254 (18) but should be augmented by varying loads. In particular, the loads used in bulkhead tests should be increased to levels on the order of $30kN/m$. Analysis methods, identical to those described in this report should be used to first predict, and subsequent to the testing verify, the methodology proposed. In particular, if possible loads of up to one-half of the ultimate design loads should be applied to bulkheads and deck panels. Complete failure is expected when the temperature T_c or T_b , whichever is applicable, is reached. In general, the analysis to be performed would predict deflections that would, in turn, be compared to those measured.

13.2 Validation *vis-a-vis* Fully 3-D Structures

A second step toward full validation would be to perform corresponding tests and analyses, using the procedures developed herein, on 3-dimensional structures. A specific purpose here would be to account for localized heating at corners or joints that will lead to extreme gradients in temperature and material degradation. Viable structures of this type would include those which are both stiffened and that contain multiple panels, in turn, joined at corners. Viable structures could include full-scale sections of compartments that would, in turn, include walls, corners, and portions of ceilings. Such sections, would be subjected to combined thermal and mechanical loading. Thermal loads could, for example, be as prescribed in the ISO 9705 room corner burn test. Mechanical loads could, for example, be prescribed as bulkheads loads and deck loads. Mechanical loads could be as used in the studies described in Section 13.1. Tests concluded on fully 3-D structures should be complemented by detailed thermal analysis as well as structural analysis. The results of these tests should be compared to the measured thermal profiles and structural responses.

13.3 Material Properties and Hybrid Materials

The methodology developed herein was based on single skin composites and cored sandwich hybrid composites. Extension of our work to more complex hybrids such as, for example, sandwich panels, syntactic foam architectures would be valuable in describing the behavior and performance of typical "T-joints" in FRP composites structures.

Complex joint geometries have hybrid material architectures that include, *inter alia*, varying sandwich panel architectures, syntactic foams of varying density, *etc.* Full-scale sections of these need to be subjected to combined thermal and mechanical testing as prescribed in the outlines contained in Sections 13.1 and 13.2.

13.4 Residual Structural Performance

Residual material properties have been measured for a range of FRP composite systems, as described in Section 2. As noted there, analytical, computational, and design methods similar to those detailed in *in-situ* fire behavior can be used. A program to perform this development, validated by the type of experiments described herein and in Sections 13.1 through 13.3 is needed to confirm the accuracy of the approach.

13.5 Structural Fire Protection Code Development

Longer range research could include the development of a complete 3-dimensional *Structural Fire Protection Code*. Such a code would be used as a design and predictive tool to assess the structural fire integrity of ship structures damaged by fire. A possible approach to this is to base such a design code on existing structural finite element codes such as ABAQUSTM or MARCTM. Such codes are design to be *user friendly* and contain a full suite of finite element types used to perform structural analysis of steel, aluminum, and FRP composite materials and structures. The proposed research would involve the development of materials modules that describe the temperature-time dependence of both *in-situ* and residual material properties. Pre-and-post-processing routines would be needed to efficiently create finite element models for head conduction and temperature field simulations; these would, in turn, create necessary constitutive data for degraded material properties. Structural analysis would then be performed and results interpreted *vis-a-vis* prescribed structural design requirements.

14 Acknowledgements

The advise of Lt. Christopher Myskowski and Lt. Kevin Oditt during the course of this study is gratefully acknowledged. The authors would also like to acknowledge Professor V. Karbhari for acquisition of data. The authors acknowledge helpful discussions with Professor Tian-Hu Hao and Dr. Pei Gu during the course of this study.

15 References

1. *International Code of Safety for High-Speed Craft* (IMO), London. 1995.
2. R.J. Asaro and M. Dao, *Marine Technology*, Vol. 34, No. 3, July 1997, pp. 197-210, Society of Naval Architects and Marine Engineers (SNAME).
3. M. Dao, R.J. Asaro and D. Alley, 1998.
4. J.R. Bernstein and J.W. Wagner, *Review of Scientific Instruments*, 68 (1997) (No. 5) 2154-7.
5. R. J. Asaro *et al.*, Research in Progress at UCSD.
6. T. McCabe, private communication, 1996.
7. J.A. Milke and A.J. Vizzini, *J. Comp. Tech. Res.*, 13 (1991), 145.
8. C.I. Chang, *Theoret. Appl. Fracture Mech.*, 6, (1986) 113.
9. C.A. Griffs, J.A. Nemes, F.R. Stonesifer and C.I. Change, *J. Comp, Mater.*, 20 (1986) 216.
10. *International Code of Safety for High-Speed Craft*, Chapter 7, International Maritime Organization (IMO), London, 1995.
11. F.R. Shanley, *J. Aero Sci.*, 14 (1947) 251.
12. H.G. Allen, *Analysis and Design of Structural Sandwich Panels*, pp. 52, Oxford, New York, Pergamon Press, 1969.
13. F.J. Plantema, *Sandwich Construction - the Bending and Buckling of Sandwich Beams, Plates, and Shells*, Chapter 2, New York, Wiley, 1966.

PROJECT TECHNICAL COMMITTEE MEMBERS

The following persons were members of the committee that represented the Ship Structure Committee to the Contractor as resident subject matter experts. As such they performed technical review of the initial proposals to select the contractor, advised the contractor in cognizant matters pertaining to the contract of which the agencies were aware, performed technical review of the work in progress and edited the final report.

Chairman

Members

Contracting Officer's Technical Representative:

Marine Board Liaison:

Executive Director Ship Structure Committee:

SHIP STRUCTURE COMMITTEE PARTNERS AND LIAISON MEMBERS

PARTNERS

The Society of Naval Architects and Marine Engineers

Mr. Bruce S. Rosenblatt
President,
Society of Naval Architects and Marine Engineers

Dr. John Daidola
Chairman,
SNAME Technical & Research Steering
Committee

The Gulf Coast Region Maritime Technology Center

Dr. John Crisp
Executive Director,
Gulf Coast Maritime Technology Center

Dr. Bill Vorus
Site Director,
Gulf Coast Maritime Technology Center

LIAISON MEMBERS

American Iron and Steel Institute
American Society for Testing & Materials
American Society of Naval Engineers
American Welding Society
Bath Iron Works
Canada Ctr for Minerals & Energy Technology
Colorado School of Mines
Edison Welding Institute
International Maritime Organization
Int'l Ship and Offshore Structure Congress
INTERTANKO
Massachusetts Institute of Technology
Memorial University of Newfoundland
National Cargo Bureau
Office of Naval Research
Oil Companies International Maritime Forum
Tanker Structure Cooperative Forum
Technical University of Nova Scotia
United States Coast Guard Academy
United States Merchant Marine Academy
United States Naval Academy
University of British Columbia
University of California Berkeley
University of Houston - Composites Eng & Appl.
University of Maryland
University of Michigan
University of Waterloo
Virginia Polytechnic and State Institute
Webb Institute
Welding Research Council
Worcester Polytechnic Institute
World Maritime Consulting, INC
Samsung Heavy Industries, Inc.

Mr. Alexander Wilson
Captain Charles Piersall (Ret.)
Captain Dennis K. Kruse (USN Ret.)
Mr. Richard Frank
Mr. Steve Tarpy
Dr. William R. Tyson
Dr. Stephen Liu
Mr. Dave Edmonds
Mr. Tom Allen
Dr. Alaa Mansour
Mr. Dragos Rauta
Mr. Dave Burke / Captain Chip McCord
Dr. M. R. Haddara
Captain Jim McNamara
Dr. Yapa Rajapaksie
Mr. Phillip Murphy
Mr. Rong Huang
Dr. C. Hsiung
Commander Kurt Colella
Dr. C. B. Kim
Dr. Ramswar Bhattacharyya
Dr. S. Calisal
Dr. Robert Bea
Dr. Jerry Williams
Dr. Bilal Ayyub
Dr. Michael Bernitsas
Dr. J. Roorda
Dr. Alan Brown
Dr. Kirsi Tikka
Dr. Martin Prager
Dr. Nick Dembsey
VADM Gene Henn, USCG Ret.
Dr. Satish Kumar

RECENT SHIP STRUCTURE COMMITTEE PUBLICATIONS

Ship Structure Committee Publications on the Web - All reports from SSC 392 and forward are available to be downloaded from the Ship Structure Committee Web Site at URL:

<http://www.shipstructure.org>

SSC 391 and below are available on the SSC CD-ROM Library. Visit the National Technical Information Service (NTIS) Web Site for ordering information at URL:

<http://www.ntis.gov/fcpc/cpn7833.htm>

SSC Report Number	Report Bibliography
SSC 440	Deterioration of Structural Integrity Due to Chemical Treatment of Ballast Water S. Tiku, 2005
SSC 439	Comparative Structural Requirements For High Speed Crafts K. Stone, 2005
SSC 438	Structural Optimization for Conversion of Aluminum Car Ferry to Support Military Vehicle Payload, R.Kramer, 2005
SSC 437	Modeling Longitudinal Damage in Ship Collisions A.J. Brown, JAW Sajdak 2005
SSC 436	Effect of Fabrication Tolerances on Fatigue Life of Welded Joints A. Kendrick, B. Ayyub, I. Assakkaf 2005
SSC 435	Predicting Stable Fatigue Crack Propagation in Stiffened Panels R.J. Dexter, H.N. Mahmoud 2004
SSC 434	Predicting Motion and Structural Loads in Stranded Ships Phase 1 A.J. Brown, M. Simbulan, J. McQuillan, M. Gutierrez 2004
SSC 433	Interactive Buckling Testing of Stiffened Steel Plate Panels Q. Chen, R.S. Hanson, G.Y. Grondin 2004
SSC 432	Adaptation of Commercial Structural Criteria to Military Needs R.Vara, C.M. Potter, R.A. Sielski, J.P. Sikora, L.R. Hill, J.C. Adamchak, D.P. Kihl, J. Hebert, R.I. Basu, L. Ferreiro, J. Watts, P.D. Herrington 2003
SSC 431	Retention of Weld Metal Properties and Prevention of Hydrogen Cracking R.J. Wong 2003
SSC 430	Fracture Toughness of a Ship Structure A.Dinovitser, N. Pussegoda, 2003
SSC 429	Rapid Stress Intensity Factor Solution Estimation for Ship Structures Applications L. Blair Carroll, S. Tiku, A.S. Dinovitser 2003
SSC 428	In-Service Non-Destructive Evaluation of Fatigue and Fracture Properties for Ship Structure S. Tiku 2003